Geochemistry Geophysics Geosystems G3

Published by AGU and the Geochemical Society

Article
Volume 14, Number 8
1 August 2013
doi: 10.1002/ggge.20134
ISSN: 1525-2027

Recent volcanic accretion at 9°N–10°N East Pacific Rise as resolved by combined geochemical and geological observations

C. L. Waters
Department of Geology and Geophysics, Woods Hole Oceanographic Institution, Woods Hole, Massachusetts, USA

Department of Geology and Geophysics, University of Wyoming, Laramie, Wyoming, USA

Now at Geosciences Research Division, Scripps Institution of Oceanography, University of California San Diego, La Jolla, California, 92093, USA (clwaters@ucsd.edu)

K. W. W. Sims
Department of Geology and Geophysics, Woods Hole Oceanographic Institution, Woods Hole, Massachusetts, USA

Department of Geology and Geophysics, University of Wyoming, Laramie, Wyoming, USA

S. A. Soule
Department of Geology and Geophysics, Woods Hole Oceanographic Institution, Woods Hole, Massachusetts, USA

J. Blichert-Toft
Laboratoire de Géologie de Lyon, Ecole Normale Supérieure de Lyon and Université Claude Bernard Lyon 1, Lyon, France

N.W. Dunbar
New Mexico Bureau of Geology & Mineral Resources, Earth and Environmental Science Department, New Mexico Tech, Socorro, New Mexico, USA

T. Plank
Lamont-Doherty Earth Observatory, Columbia University, Palisades, New York, USA

J. Prytulak
Department of Earth Science and Engineering, Imperial College, London, UK

Bristol Isotope Group, Department of Earth Sciences, University of Bristol, UK

R. A. Sohn
Department of Geology and Geophysics, Woods Hole Oceanographic Institution, Woods Hole, Massachusetts, USA

M. A. Tivey
Department of Geology and Geophysics, Woods Hole Oceanographic Institution, Woods Hole, Massachusetts, USA

[1] The ridge crest at 9°N–10°N East Pacific Rise (EPR) is dominated by overlapping lava flows that have overflowed the axial summit trough and flowed off-axis, forming a shingle-patterned terrain up to ~2–4 km on either side of the axial summit trough. In this study, we employ ^{230}Th-^{226}Ra dating methods, in conjunction with geochemistry and seafloor geological observations, in an effort to discern the stratigraphic relationships between adjacent flows. We measured major and trace elements and ^{87}Sr/^{86}Sr,

$^{143}Nd/^{144}Nd$, $^{176}Hf/^{177}Hf$, and ^{238}U-^{230}Th-^{226}Ra for lava glass samples collected from several flow units up to ~2 km away from the axial summit trough on the ridge crest at 9°50′N EPR. Statistical analysis of the ^{238}U-^{230}Th-^{226}Ra data indicates that all but one measured sample from these flows cannot be resolved from the zero-age population; thus, we cannot confidently assign model ages to samples for discerning stratigraphic relationships among flows. However, because groups of samples can be distinguished based on similarities in geochemical compositions, particularly incompatible element abundances with high precision-normalized variability such as U and Th, and because the range of compositions is much greater than that represented by samples from the 1991–1992 and 2005–2006 eruptions, we suggest that the dive samples represent 6–10 eruptive units despite indistinguishable model ages. Geochemical variability between individual flows with similar ages requires relatively rapid changes in parental melt composition over the past ~2 ka, and this likely reflects variations in the relative mixing proportions of depleted and enriched melts derived from a heterogeneous mantle source.

Components: 18,839 words, 9 figures, 5 tables.

Keywords: U-series; geochemistry; geochronology; East Pacific Rise.

Index Terms: 3035 Marine Geology and Geophysics: Midocean ridge processes; 1120 Geochronology: Isotopic disequilibrium dating; 8416 Volcanology: Mid-oceanic ridge processes; 3619 Mineralogy and Petrology: Magma genesis and partial melting.

Received 30 January 2013; **Revised** 14 March 2013; **Accepted** 26 March 2013; **Published** 1 August 2013.

Waters, C. L., K. W. W. Sims, S. A. Soule, J. Blichert-Toft, N. W. Dunbar, T. Plank, J. Prytulak, R. A. Sohn,, M. A. Tivey, (2013), Recent volcanic accretion at 9°N–10°N East Pacific rise as resolved by combined geochemical and geological observations, *Geochem. Geophys. Geosyst., 14*, 2547–2574, doi:10.1002/ggge.20134.

1. Introduction

[2] Mid-ocean ridge spreading at the East Pacific Rise (EPR) from 9°N to 10°N typically has been viewed as a geologically continuous process involving eruptions and dike emplacement within a narrow zone of magmatism defined by the axial summit trough (Figure 1) [*Fornari et al*., 1998; *Gregg et al*., 1996; *Haymon et al*., 1991, 1993; *Perfit and Chadwick*, 1998; *Schouten et al*., 2001, 2002; *Sims et al*., 2002, 2003; *Soule et al*., 2009]. However, seismic studies suggest that seismic layer 2A, interpreted as the extrusive crust, doubles in thickness within ~2–4 km from the axial summit trough [*Christeson et al*., 1994, 1996; *Harding et al*., 1993; *Schouten et al*., 1999; *Sohn et al*., 2004; *Vera and Diebold*, 1994], requiring that a significant component of volcanic crustal accretion occurs outside of this region [*Goldstein et al*., 1994; *Hooft et al*., 1996; *Kurras et al*., 2000; *Perfit et al*., 1994; *Sims et al*., 2003; *Soule et al*., 2005; *White et al*., 2002]. Magnetic surveys, Autonomous Benthic Explorer (ABE) 675 kHz microbathymetry, and DSL-120A side-scan sonar imagery in the 9°50′N region reveal that a highly magnetized and high acoustic backscatter region defined as the "neo-volcanic zone" extends to ~2–4 km on either side of the axial summit trough and is dominated by a shingle-patterned lava terrain (Figure 2) [*Fornari et al*., 2004, Plate 2; *Schouten et al*., 1999; *Sims et al*., 2003, Figure 1b; *Williams et al*., 2008]. Consequently, the neo-volcanic zone appears to be produced primarily by transport of lavas away from the axial summit trough, either from lava overflow of the axial summit trough or flow through subterranean tubes [*Fornari et al*., 2004; *Haymon et al*., 1993; *Kurras et al*., 2000; *Soule et al*., 2005]. This inference is consistent with more recent studies of an eruption in 2005–2006 that show that, in places, lava flowed up to ~3 km from the axial summit trough (Figure 1) [*Fundis et al*., 2010; *Soule et al*., 2007]. Off-axis pillow mounds, which have also been proposed to contribute to extrusive layer thickening [*Perfit et al*., 1994], appear to make up a less significant component of neo-volcanic zone accretion [cf., *Sims et al*., 2003, Figure 1b].

[3] Although high-resolution spatial observations can elucidate the mechanisms of volcanic accretion, they are limited in their ability to quantify temporal aspects of ridge evolution. For example, sediment thickness variations can be useful for making first-order observations of relative lava ages for lava flows of significantly different ages and sediment

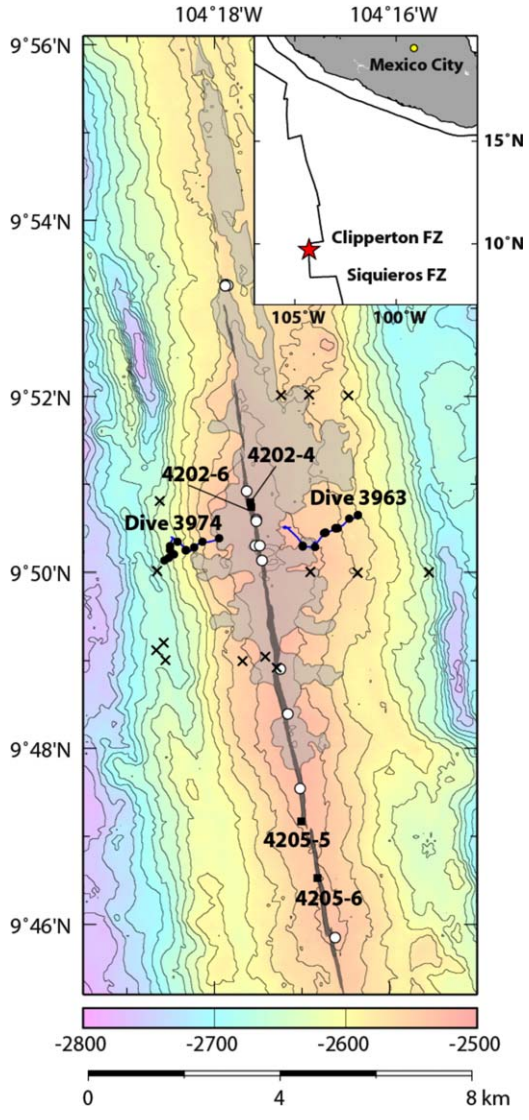

Figure 1. EM300 bathymetric map of the region from 9°45′N to 9°56′N EPR [*White et al*., 2006] showing sample locations and dive tracks for *Alvin* dives 3974 and 3963 as well as locations for samples analyzed from the 2005–2006 eruption (dives 4202, 4205). A gray line shows the location of the axial summit trough, and the shaded field shows the mapped extent of the 2005–2006 eruption. Note that the along-axis extent of the 1991–1992 eruption was roughly similar to the 2005–2006 eruption and it was not believed to have flowed more than a few hundred meters from the axial summit trough in any location and in most places only filled the axial summit trough [*Haymon et al*., 1993; *Gregg et al*., 1996]. Open circles show axial samples analyzed by *Sims et al*. [2002]; crosses indicate samples analyzed by *Sims et al*. [2003]. Contour interval is 20 m. Inset map locates the study area, 9°N to 10°N, along the East Pacific Rise (EPR).

cover. However, absolute ages of lava flows in years or relative ages of similarly sedimented lava flows estimated from sediment thicknesses are less reliable due to differences in sediment appearances on different lava morphologies (flat surfaces generally appear more sedimented than textured surfaces) as well as local variations in deposition from hydrothermal venting and sediment winnowing by deep ocean currents [e.g., *Ballard et al*., 1979; *Cann and Smith*, 2005; *Perfit and Chadwick*, 1998]. As a result, little is known about the age and compositional and stratigraphic relationships among adjacent "shingles" (interpreted to be lava flow lobes) within the neo-volcanic zone; yet, this information is necessary for determining whether the shingled terrain is produced by the overlapping of flows from multiple eruptions sourced within the axial summit trough or elsewhere, or reflects ridge crest repaving by single, large eruptions. This type of information is crucial for understanding the processes that produce the neo-volcanic zone at fast-spreading ridges, and it has important implications for spreading-rate dependent models of mid-ocean ridge behavior (e.g., it is presumed that fast-spreading ridges produce smaller volume eruptions than intermediate- and slow-spreading ridges, *Sinton et al*. [2002]).

[4] Determining stratigraphic relationships among mid-ocean ridge lava flows and eruptive units using solely submersible/geological observations can be problematic due to logistical difficulties (e.g., limitations in dive time, areal coverage, field of view, and area of illuminated seafloor), variability in sedimentation, and the overall complexity of volcanic terrain (e.g., tube flow and localized breakouts through the flow front; intraflow variations in lava morphology; superposition and interfingering of flow units or flow lobes; braiding of lava tubes and channels within flows; ponding or channeling of flows due to faulting and topography) [e.g., *Ballard et al*., 1979; *Cann and Smith*, 2005; *Escartin et al*., 2007; *Fornari et al*., 2004; *Fundis et al*., 2010; *Gregg and Fink*, 1995, 2000; *Hon et al*., 1994; *Thordarson and Self*, 1993]. When combined with geological and remote sensing observations, lava geochemistry can be critical for distinguishing among different lava flows. However, because geochemical variability is known to exist within flows of both individual submarine [*Bergmanis et al*., 2007; *Goss et al*., 2010; *Perfit and Chadwick*, 1998; *Rubin et al*., 2001; *Sims et al*., 2002] and subaerial basaltic eruptions [e.g., *Maclennan et al*., 2003; *Rhodes*, 1983], and because lava flow compositions are nonunique and may recur over time, particularly in an area with lava as homogeneous as 9°50′N EPR, lava age is a key parameter for identifying distinct eruptive episodes and thus determining lava stratigraphy. An interesting counterpoint to observations of geochemical heterogeneity within mid-ocean ridge

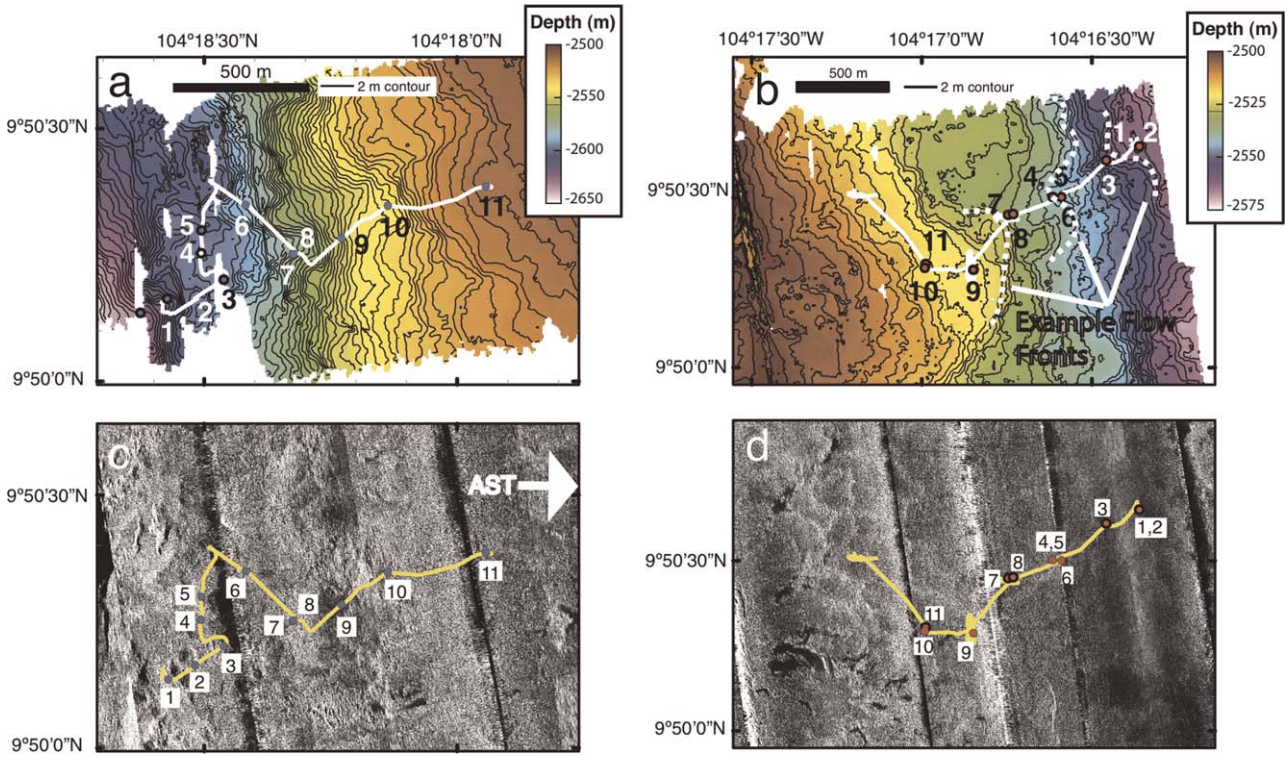

Figure 2. Microbathymetric maps from ABE surveys [*Fornari et al*., 2004] of the (a) *Alvin* dive 3974 and (b) *Alvin* dive 3963 study areas showing sample locations and dive tracks. DSL-120A side-scan sonar maps [*Escartin et al*., 2007; *Fornari et al*., 2004] of the (c) *Alvin* dive 3974 and (d) *Alvin* dive 3963 study areas. The dive tracks are shown as white or yellow lines that connect blue and red, numbered sample locations. Inferred flow fronts are shown as dashed white lines in Figure 2b. Note the different scales in Figures 2a and 2c versus Figures 2b and 2d.

type flows is the extremely voluminous (~15 km^3) 1783–1784 Laki eruption in Iceland that displayed remarkably homogeneous abundances of Th (1.12 ± 0.02 ppm (2σ), n =11) and U (0.344 ± 0.007 ppm (2σ), n =11), Th/U (3.27 ± 0.01), $^{87}Sr/^{86}Sr$ (0.70324, n=3), and $\delta^{18}O$ (3.13 ‰, n=4) [*Sigmarsson et al*., 1991].

[5] Uranium decay series (U-series) dating techniques provide a more accurate means for dating mid-ocean ridge basalts (MORB) on time scales of ~0.1–375 ka [*Cooper et al*., 2003; *Goldstein et al*., 1992, 1993, 1994; *Lundstrom*, 2003; *Rubin and MacDougall*, 1990; *Rubin et al*., 1994; *Sims et al*., 2003; *Standish and Sims*, 2010; *Sturm et al*., 2000; *Waters et al*., 2011; *Elkins et al*., 2011]. The presence or absence of disequilibria between daughter and parent nuclides (e.g., ^{238}U-^{230}Th-^{226}Ra-^{210}Pb, and $^{235}U^{-231}Pa$) can place absolute age limits on lava samples, and under certain conditions disequilibria can provide finer temporal resolution by model age dating. *Sims et al*. [2003] used U-series model ages at 9°50′N EPR to show that volcanic construction is not limited to the axial summit trough and occurs over the full width of the neo-volcanic zone, which is consistent with both geological and geophysical observations [*Christeson et al*., 1994, 1996; *Fornari et al*., 2004; *Harding et al*., 1993; *Hooft et al*., 1996; *Perfit and Chadwick*, 1998; *Perfit et al*., 1994; *Schouten et al*., 1999; *Sohn et al*., 2004]. However, this study did not provide sufficient geographical coverage to identify age relationships between adjacent lava flows. We addressed this issue by collecting new sample suites from 9°N to 10°N EPR using the *DSV Alvin* during the cruise AT11-7 in 2004 that were explicitly identified to have come from different flow lobes (i.e., shingles). Samples were collected along two dive transects (dives 3963 and 3974) that traversed the east and west sides of the ridge crest from ~0.7 to 2.0 km from the axial summit trough, spanning a major portion of the neo-volcanic zone (Figures 1–3) [*Schouten et al*., 2004]. These samples were collected directly from pillow lavas and adjacent lobate and sheet flows that correspond to, respectively, the fronts and bodies of flow shingles observed in side-scan sonar and ABE

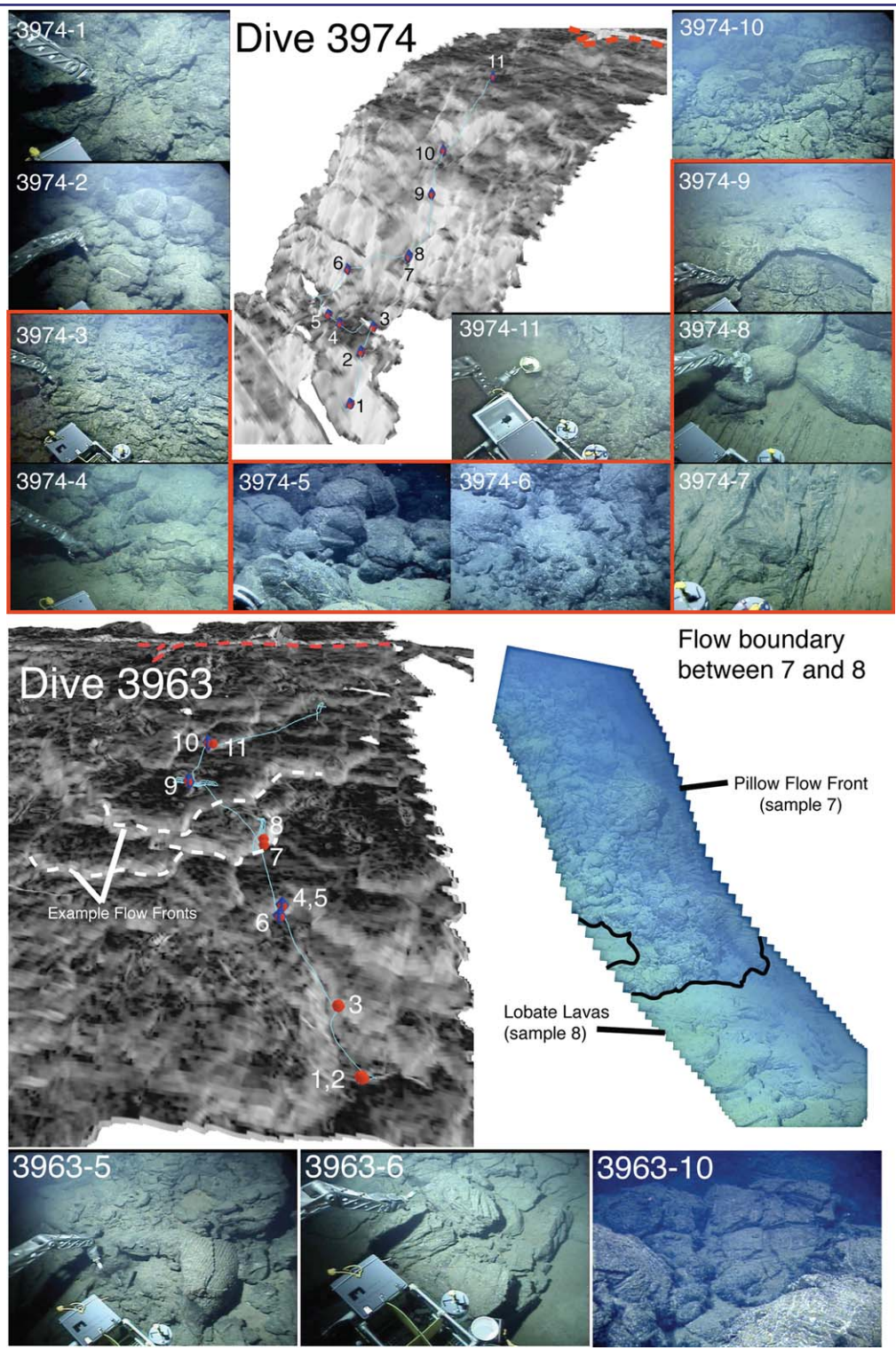

Figure 3. Perspective ABE bathymetric maps of dives (a) 3974 and (b) 3963. Dive tracks are shown as cyan lines. Images are vertically exaggerated to better show the 5–15 m high-flow fronts (VE estimated at ~7×). Light shades indicate steep slopes (e.g., pillow flow fronts); dark areas indicate relatively flat areas (e.g., lobate and sheet flows). Dashed red lines mark the axial summit trough boundary. Sample locations are marked with numbered circles, and digital images of selected sample sites are provided for context. Samples dated using ^{230}Th-^{226}Ra model ages are further denoted by dark blue diamonds. Red outlines group photos of geochemically similar samples (see text for details). A photomosaic of a characteristic flow boundary observed during dive 3963 between samples 3963-7 and 3963-8, constructed using the ALVIMOS software [*Rhzanov et al.*, 2006], is shown to the right of the dive 3963 map. The field of view is estimated to be ~2–3 m for photos of 3963-5, 6, 10, and 3974-2, 3, 4, 5, 6, 8, 9, 10, and 11 and ~1.5 m for 3974-1 and 3974-7 (note that the lasers are 10 cm apart).

Table 1. Sample Descriptions for *Alvin* Dives 3963 and 3974

Sample	Time of Collection[a]	Latitude (°N)	Longitude (°W)	Depth (m)	Flow Type	Geologic Context (Dive Observations)
3963-1	16:45	9°50.653'	104°16.360'	2562	Sheet	From *Alvin* touchdown area ~2.2 km east of AST, before first flow front.
3963-3	17:54	9°50.610'	104°16.458'	2557	Pillow	Flow front #1. To west and south of samples 1 and 2.
3963-4	18:15	9°50.502'	104°16.615'	2542	Pillow	Flow front #2. Same location as sample 5 –probably the same lava. Appears younger than 3963-6.
3963-5	18:16	9°50.502'	104°16.615'	2543	Pillow	Flow front #2. Same location as sample 4—probably same lava. Looks like a drained tube. Appears younger than 3963-6. Area is structurally disrupted with many slabs of crusts.
3963-6	18:32	9°50.501'	104°16.589'	2544	Sheet	Between flow front #1 and flow front #2. Part of lobate/sheet area to east of 3963-4 and −5. Underlies 3963-4 and −5. Complicated area of collapses and sheet flows.
3963-7	18:47	9°50.450'	104°16.746'	2532	Pillow	Flow front #3. Knobbly pillow flow front; appears younger than 3963-4 & −5. Overlies 3963-8. Less sediment here.
3963-8	19:25	9°50.452'	104°16.731'	2534	Lobate	To east and below 3963-7.
3963-9	19:45	9°50.288'	104°16.848'	2524	Sheet	Sheet flow from edge of 1m high channel. Not clear if this sample is from the channel itself or from a collapsed channel above.
3963-10	20:36	9°50.294'	104°16.991'	2517	Pillow	Flow front #4. North and west of previous samples. Flow front is over lobate terrain that may be related to the channel sample 3963-9.
3963-11	20:43	9°50.305'	104°16.989'	2518	Pillow	Flow front #4. Same flow front as #10. Sampled very glassy toe of flow.
3974-1	17:40	9°50.136'	104°18.571'	2603	Sheet	From *Alvin* touchdown area ~2 km west of the AST. Field of jumbled and hackly sheet flows in a low area west of the first flow front.
3974-2	18:00	9°50.164'	104°18.518'	2594	Pillow	Flow front #1. Lava from first flow front to the east of 3974-1. May be part of a pillow mound on the flow front.
3974-3	18:23	9°50.202'	104°18.461'	2595	Sheet	Hackly sheet flow taken from just after the pillows.
3974-4	18:47	9°50.254'	104°18.506'	2598	Lobate	Tubular flow in a terrain of mixed sheets and lobates.
3974-5	19:16	9°50.299'	104°18.505'	2599	Pillow	Flow front #2. From above 3974-4 on rise of flow front.
3974-6	19:47	9°50.349'	104°18.418'	2579	Pillow	Flow front #2. Taken from foot of flow.
3974-7	20:16	9°50.251'	104°18.326'	2569	Sheet	Flow on flat area to the west of flow front #2. Pillow 3974-6 may be younger/over this sample.
3974-8	20:26	9°50.252'	104°18.323'	2568	Pillow	Flow front #2(?). In contact with and directly overlying the sheet flow sampled by 3974-7. May be the same unit as 3974-6.
3974-9	20:50	9°50.386'	104°18.229'	2546	Lobate	Flow body #2. Taken from a field of lobate lava on plateau over flow front #2.
3974-10	21:14	9°50.284'	104°18.137'	2532	Pillow	Flow front #3. Sampled from a 10–15 m high flow front. Over sample 3974-9.
3974-11	21:55	9°50.348'	104°17.943'	2517	Lobate	Sampled from large flat area about 700 m east of the AST

[a]All dive 3963 samples were collected on 4 Feb. 2004; dive 3974 samples were collected on 17 Feb. 2004. Time is reported as Greenwich Mean Time.

microbathymetry, and they provide more appropriate sample spacing and continuity for determining the geochemical and age relationships among a stratigraphically related series of flow units.

[6] In this study, we combine geological and remote sensing observations, U-series age constraints, and geochemical and isotopic data in an effort to unravel volcanic stratigraphy along the ridge crest at 9°50′N EPR. We evaluate the resolution of the U-series model age techniques, namely ^{230}Th-^{226}Ra model age dating, for dating dive 3974 and 3963 samples, as exact age determinations have the potential to provide the strongest complementary constraints to geological observations of complex volcanic stratigraphy. In addition, we examine the geochemical variability in dive 3974 and 3963 samples and compare this to data for the 1991–1992 and 2005–2006 eruptions, which currently provide the best constraints on the degree of intra- and inter-eruption natural geochemical variability at 9°50′N EPR. Finally, we evaluate the relative utility of each method and how coupling of these independent constraints might lead to a more comprehensive understanding of ridge crest volcanic accretionary processes.

2. Background

2.1. Sample Locations and Descriptions

2.1.1 Samples from Dives 3963 and 3974

[7] Lava samples were collected at and between inferred lava flow fronts up to ~2 km to the east and west side, respectively, of the axial summit trough at ~9°50′N (Figures 1–3). Observations of lava morphology and qualitative age indicators were made along the dive tracks. Microbathymetry (from ABE), shipboard multibeam bathymetry (EM300), and high-resolution sidescan sonar imaging (DSL-120A) are also

available for this area [*Cochran et al*., 1999; *Fornari et al*., 1998, 2004]. It is important to note that these samples, and the accompanying remote sensing data that we present in the figures in this study, were collected prior to the 2005–2006 eruption, although most of the flows we sampled were not covered by flows erupted in 2005–2006 (Figure 1). Dive track and sample locations are shown in Figures 1–3. *In situ* dive observations, hand sample descriptions, and the morphology of the lavas from which samples were collected are summarized in Table 1. Dive summaries can be found in Appendix A (from supporting information).[1]

2.1.2 Samples from the 2005–2006 Eruption

[8] We analyzed ^{238}U-^{230}Th-^{226}Ra disequilibria for four samples previously acquired by *DSV Alvin* during dives 4202 and 4205 from flows associated with the 2005–2006 eruption near 9°50′N EPR (Figure 1) [*Goss et al*., 2010; *Rubin et al*., 2008; *Soule et al*., 2007]. These recently erupted samples provide additional constraints on the initial disequilibria of zero-age lavas at this site and augment the zero-age trend previously established for samples erupted during 1991–1992 [*Sims et al*., 2002]. Major and trace element and Sr, Nd, and Pb isotope data reported by *Goss et al*. [2010] further provide constraints on the geochemical variability from a single eruption. These samples were also analyzed for U and Th abundances by isotope dilution (ID) and U and Th isotopic compositions at the University of Bristol and for U and Th ID abundances at the University of Wyoming for purposes of interlaboratory comparison (see Appendix B; supporting information). For simplicity, and because the WHOI data appear reproducible, we plot only WHOI U-series data in the figures.

2.1.3. Previously Analyzed Samples from the 1991–1992 Eruption and Additional Samples from 9°48′N to 9°52′N

[9] Samples collected from within the axial summit trough from 9°17′ to 9°54′N, including a number of samples determined by ^{210}Po ingrowth to have erupted in 1991 and 1992 [*Rubin et al*., 1994], have been previously measured for major and trace elements, Sr, Nd, Pb, and Hf isotope compositions, and U-series disequilibria [*Rubin et al*., 2005; *Sims et al*., 2002]. In addition, *Sims et al*. [2003] similarly analyzed a suite of samples from the ridge crest between 9°48′N and 9°52′N EPR. Sample locations are shown in Figure 1 for geographic comparison to the samples from dive 3963, dive 3974, and the 2005–2006 eruption.

2.2. Dating Lavas with U-Th-Ra Disequilibria

[10] Uranium-series dating techniques have been used for dating MORB on time scales of ~0.1–375 ka [*Cooper et al*., 2003; *Goldstein et al*., 1992, 1993, 1994; *Lundstrom*, 2003; *Rubin and MacDougall*, 1990; *Rubin et al*., 1994; *Sims et al*., 2003; *Standish and Sims*, 2010; *Sturm et al*., 2000; *Waters et al*., 2011; *Elkins et al*., 2011]. Prior to partial melting of the mantle source, the nuclides in the U-series decay chain are assumed to be in secular equilibrium, such that the activities of the constituent U-series nuclides are equal and their activity ratios (herein denoted by parentheses) are equal to unity. However, because the U-series decay chain is composed of elements that have different partition coefficients (in particular U, Th, and Ra) [e.g., *Beattie*, 1993; *Blundy and Wood*, 2003; *Elkins et al*., 2008; *Hauri et al*., 1994; *LaTourette et al*., 1993; *Pertermann et al*., 2004; *Salters and Longhi*, 1999; *Salters et al*., 2002], magmatic processes, primarily partial melting and melt transport, may fractionate these elements and perturb the steady-state condition [cf., *Elliot*, 1997; *McKenzie*, 1985; *Spiegelman and Elliot*, 1993]. After fractionation ceases, secular equilibrium is reached again in roughly five half-lives, or ~8 ka for ^{226}Ra ($t_{1/2}$=1.6 ka) and ~375 ka for ^{230}Th ($t_{1/2}$=75 ka). This time includes both time spent on the seafloor following eruption and any time spent during melt transport through the mantle and crust after cessation of fractionation, including crustal residence in magma chambers prior to eruption. Thus, measurable disequilibrium, for example (^{226}Ra/^{230}Th) $\neq 1.00 \pm 0.05$ (2SE), or (^{230}Th/^{238}U) $\neq 1.00 \pm 0.02$ (2SE), can be used to constrain the maximum eruption age of a given lava to approximately 8 ka or 375 ka, but incorporates some component of pre-eruptive decay.

[11] Furthermore, if the initial extent of disequilibrium in a basalt sample upon eruption can be established, then the difference between the initial and measured disequilibrium of a lava of unknown age potentially can be used to estimate more precisely the lava eruption age, implicitly taking into account magma transport and residence times. Uranium-series model ages for MORB have been calculated in this way by estimating the initial ^{238}U-^{230}Th-^{226}Ra disequilibria from data for the

[1]Additional supporting information may be found in the online version of this article.

youngest axial basalts (e.g., lava erupted in 1991–1992) and comparing these with disequilibria measured in samples of unknown age [*Goldstein et al*., 1993, 1994; *Rubin and MacDougall*, 1990; *Sims et al*., 2003; *Volpe and Goldstein*, 1993; *Waters et al*., 2011]. However, because U-series model ages assume that the initial disequilibria in the sample upon eruption was equal to that in lavas of known age, calculating reliable model ages requires that the petrogenetic processes that generated the U-series disequilibria in lavas of unknown age (to be dated) were similar to the processes that generated disequilibria in zero-age lavas, and that the lavas remained a closed system with respect to Th/U after eruption [*Sims et al*., 2003]. In the present study, this means that lavas from the 1991–1992 and 2005–2006 eruptions experienced the same degree of ^{238}U-^{230}Th-^{226}Ra fractionation due to partial melting processes and subsequent decay during magma transport and residence as dive 3974 and 3963 lavas, and that mixing processes are either identical or can be accounted for rigorously. Consequently, complexity in magmatic processes that cannot be accounted for, as well as petrologic and geochemical differences between lavas of known age and lavas to be dated, can lead to unknown uncertainties in the accuracy of calculated model ages. For example, how similar residence times are for samples (e.g., *Rubin et al*. [2005] discuss the possibility of crustal mixing of melts with short (44–66 years) and long (~200–400 years) residence times) or exactly when or where magma mixing processes occur, remain difficult to constrain generally or for specific eruptions, even at a ridge segment as well studied as 9°N to 10°N EPR. However, such short residence times will result in only small differences in ^{230}Th-^{226}Ra model ages (^{226}Ra half-life is ~1.6 ka), but the ability to account for these small variations would undoubtedly result in higher precision age estimates. Because of the uncertainties listed above, a shortcoming of the model age technique is that its proper application at any ridge segment requires thorough, prior assessment of local processes contributing to variability in initial U-series disequilibria. Regardless, U-series model ages remain one of the most useful methods for estimating the ages of young MORB, and continued refinement of the techniques can only be improved by additional petrogenetic and U-series studies of MORB.

2.3. Mapping From Variations in Lava Geochemistry

[12] Previous studies have attempted to use major element and $TiFe_X$ compositional variations to map variations in mid-ocean ridge magma chemistry over time [e.g., *Perfit et al*., 1994; *Reynolds et al*., 1992], implicitly assuming that such variations can be used to distinguish among flows generated from different eruptions. ($TiFe_X$ was defined as the sum of the differences of 1.5 × Ti and Fe concentrations from their means after correcting Ti and Fe for crystal fractionation to a constant MgO of X, where X=8.0 wt% [*Perfit et al*., 1994] and 7.3 wt% [*Reynolds et al*., 1992]). However, *Rubin et al*. [2001] demonstrated that substantial major element geochemical heterogeneity exists within individual eruptions at mid-ocean ridges. They also noted that $TiFe_X$ in the reported MORB populations exhibits only two [*Perfit et al*., 1994] to three [*Reynolds et al*., 1992] times the variability of the quoted precision of $TiFe_X$ ($\pm$0.4, 2σ), which is similar to the precision-normalized natural variability found within individual eruptions from other parts of the global mid-ocean ridge system. This observation indicates that geochemical mapping can be ambiguous unless the precision-normalized variability is large [cf., *Sinton et al*., 2002], and it highlights the need for choosing geochemical metrics with variability that is large compared to measurement precision and natural variability in individual flows. In addition, evaluating precision-normalized variability is crucial for choosing geochemical metrics that can best resolve natural variability over analytical uncertainties for the purpose of discriminating between individual lava flows. Furthermore, because individual subaerial and submarine basaltic eruptions are known to exhibit geochemical variability [e.g., *Bergmanis et al*., 2007; *Goss et al*., 2010; *Maclennan et al*., 2003; *Perfit and Chadwick*, 1998; *Rhodes*, 1983; *Rubin et al*., 1994, 2001, 2005; *Sims et al*., 2002], the importance of choosing metrics with high precision-normalized variability becomes even more important.

3. Results

3.1. Major and Trace Elements

[13] Major and trace element compositions and analytical method details are reported in Tables 2 and 3. All measured lava samples are low-K, tholeiitic, incompatible element-depleted normal MORB (N-MORB; $K_2O/TiO_2 \times 100 < 11$; *Smith et al*. [2001]), but dive 3974 and 3963 samples extend to slightly higher values of $K_2O/TiO_2 \times 100$ (6.6–10.8 $\pm$ 14.1% (2σ)) compared to previously measured samples from the 1991–1992 (5.8–9.6; *Sims et al*. [2002]) and 2005–2006 eruptions (6.1–8.9; *Goss et al*. [2010]). Molar Mg# ($Mg'/(Mg'+0.9Fe')$ × 100) $\pm$ 2.7% (2σ) for dive 3963 samples cluster around two distinct values

Table 2. Major Element Compositions of Dive 3963, Dive 3974, and 2005–2006 Lavas Collected from 9°50′N EPR[a]

Sample	SiO_2	TiO_2	Al_2O_3	MgO	CaO	MnO	FeO^T	Na_2O	K_2O	P_2O_5	SO_2	F	Cl	Total	Mg#	K/Ti
3974-1	50.50	1.55	15.03	7.58	11.83	0.19	10.49	2.73	0.11	0.14	0.22	0.04	0.00	100.42	52.9	6.8
3974-2	50.48	1.52	15.02	7.48	11.71	0.19	10.41	2.71	0.10	0.13	0.21	0.05	0.01	100.01	52.7	6.6
3974-3	50.37	1.38	15.46	8.01	12.06	0.18	9.80	2.57	0.12	0.11	0.20	0.05	0.00	100.30	57.9	9.0
3974-4	50.54	1.41	15.49	7.90	12.05	0.17	9.86	2.60	0.12	0.12	0.21	0.05	0.01	100.52	57.0	8.7
3974-5	50.35	1.55	15.23	7.61	11.79	0.18	10.19	2.75	0.16	0.18	0.22	0.04	0.01	100.26	54.2	10.6
3974-6	50.56	1.55	15.34	7.60	11.83	0.18	10.06	2.72	0.16	0.17	0.23	0.07	0.01	100.47	54.7	10.2
3974-7	50.38	1.40	15.75	8.15	12.02	0.17	9.74	2.62	0.15	0.13	0.22	0.02	0.01	100.76	58.8	10.5
3974-8	50.33	1.38	15.81	7.87	11.98	0.18	9.65	2.63	0.14	0.12	0.21	0.05	0.01	100.35	57.8	10.5
3974-9	50.06	1.38	15.69	8.23	11.95	0.16	9.64	2.63	0.14	0.16	0.21	0.04	0.01	100.30	59.6	10.0
3974-10	50.34	1.28	15.74	8.08	12.09	0.19	9.52	2.59	0.11	0.14	0.21	0.08	0.00	100.38	59.4	8.4
3974-11	50.26	1.29	15.79	8.48	12.13	0.13	9.67	2.54	0.11	0.11	0.19	0.03	0.00	100.75	60.8	8.4
3963-3	50.47	1.54	14.88	7.39	11.92	0.18	10.24	2.70	0.13	0.12	0.21	0.09	0.01	99.88	52.9	8.7
3963-5	50.55	1.45	14.88	7.43	11.99	0.20	10.19	2.67	0.16	0.13	0.22	0.02	0.01	99.89	53.3	10.8
3963-6	50.45	1.46	15.00	7.69	12.02	0.16	10.21	2.65	0.13	0.12	0.21	0.07	0.01	100.18	54.6	8.6
3963-9	49.84	1.08	16.08	8.74	12.20	0.16	9.08	2.40	0.08	0.09	0.18	0.09	0.01	100.01	64.8	7.2
3963-10	49.76	1.11	16.54	8.67	12.12	0.15	8.98	2.46	0.09	0.09	0.16	0.07	0.01	100.22	64.9	8.2
4202-4	50.43	1.37	15.40	8.00	11.88	0.17	10.06	2.71	0.11	0.10	0.22	0.06	0.01	100.50	56.7	7.8
4202-6	50.39	1.36	15.28	8.23	11.72	0.17	9.99	2.66	0.10	0.14	0.21	0.04	0.01	100.29	58.2	7.0
4205-5	50.43	1.41	15.17	7.85	11.98	0.18	10.15	2.67	0.10	0.14	0.23	0.07	0.01	100.39	55.6	7.2
4205-6	50.51	1.47	15.26	7.68	11.86	0.15	10.08	2.66	0.10	0.12	0.23	0.06	0.01	100.19	55.0	6.9
Standards																
ALV2392-9																
Measured (n=9)	49.97	1.24	15.68	8.47	12.07	0.17	9.50	2.59	0.09	0.12	0.21	0.07	0.00	100.17		
Accepted	50.04	1.31	15.48	8.50	12.15	0.18	9.38	2.56	0.09	0.13				99.81		
Rel. Accuracy (%)	0.14	5.37	−1.30	0.32	0.68	6.91	−1.31	−1.02	3.70	10.17						
±2 σ (n=9)	0.41	0.06	0.14	0.15	0.16	0.05	0.20	0.11	0.04	0.08	0.04	0.12	0.01			
VG-2																
Measured (n=6)	50.65	1.82	14.03	6.81	10.68	0.23	11.77	2.67	0.19	0.20	0.24	0.09	0.03	99.41		
Accepted	50.81	1.85	14.06	6.71	11.12	0.22	11.82	2.62	0.19	0.20				99.60		
Rel. Accuracy (%)	0.32	1.62	0.22	−1.47	4.12	−4.00	0.41	−1.71	−1.64	−1.88						
±2 σ (n=6)	0.38	0.10	0.15	0.12	0.30	0.11	0.24	0.18	0.03	0.08	0.07	0.13	0.02			

[a]Major element compositions were measured on polished glass chips at the New Mexico Bureau of Geology and Mineral Resources in Socorro, NM using a Cameca SX100 electron microprobe. Individual spots were analyzed with an accelerating voltage of 15 kV, a beam current of 10 nA, a beam diameter defocused to 20 μm to avoid Na loss during analysis, and a count time of 20 s for all elements except for F, S, and Cl, which were counted for 60, 40, and 40 s, respectively. Analyses of six to nine separate points on two to three chips of the same sample were averaged for each sample. Accuracy was monitored by repeated runs of Smithsonian microprobe glass standard VG-2, a MORB glass from the Juan de Fuca ridge [*Jarosewich et al*., 1980], and ALV2392-9, a MORB glass from the 1991–1992 eruption at 9°50′N EPR [*Sims et al*., 2002]. Accuracy is reported as relative error (%) and reproducibility is given by 2σ standard deviation. It is important to note that although CaO appears anomalously low for VG-2 with respect to the accepted value, the mean of 40 points from 10 randomly selected reference material runs over the past 6 years is 10.8 ±0.1, confirming that the VG-2 standard used at NMBGMR does indeed have lower CaO than the accepted value. Mg# = molar Mg/(Mg+0.9 × Fe); K/Ti = K_2O/TiO_2 × 100.

with the samples furthest from the axial summit trough (3963-3, 5, and 6) having Mg#∼53–55 and the samples closest to the axial summit trough (3963-9 and 3963-10) having Mg#∼65 (Figure 4a, Table 2). Dive 3974 samples have a more continuous distribution of Mg#∼53–61, with pillowed flow fronts having generally lower Mg# than flow bodies. In both dives, the lavas closest to the axial summit trough are the most primitive, with the more evolved lavas being located farther from the axial summit trough (Figure 4a). Samples from the 2005–2006 eruption measured in this study have K_2O/TiO_2 × 100 ∼6.9–7.8 and Mg# ∼55–58. In comparison, previously reported samples from the 1991–1992 and 2005–2006 eruptions have Mg# ∼58–66 [*Sims et al*., 2002] and Mg# ∼59–64 [*Goss et al*., 2010], respectively.

[14] Dive 3963 samples also have trace element abundances that cluster in two distinct groups, with the more primitive samples 3963-9 and 3963-10 having slightly lower abundances of incompatible elements, and the more evolved samples 3963-3, −5, and −6 having higher abundances of incompatible elements (Figure 4). Dive 3974 lavas show a more continuous distribution of incompatible element abundances, although incompatible element abundances and ratios do not appear to be correlated with Mg# (Figure 4). Samples 3974-5, 6, 7, 8, and 9 have higher incompatible element ratios (e.g., Ba/Y × 100 = 41–57 ± 4.6% (2σ)) than the other dive 3974 samples (Ba/Y × 100 = 18–32), implying more enriched parental melt compositions for these lavas.

3.2. Sr, Nd, and Hf Isotopes

[15] Sample $^{87}Sr/^{86}Sr$, $^{143}Nd/^{144}Nd$, and $^{176}Hf/^{177}Hf$ are reported in Table 4; the details of the analytical methods are given in the table

Table 3. Trace Element Compositions of Dive 3963, Dive 3974, and 2005–2006 Lavas Collected From 9°50′N EPR[a]

Sample	3974-1	3974-2	3974-3	3974-4	3974-5	3974-6	3974-7	3974-8	3974-9	3974-10	3974-11
Li	6.59	5.72	6.07	7.03	6.68	5.86	6.22	6.15	6.04	5.88	6.91
Be	0.628	0.604	0.612	0.591	0.622	0.635	0.622	0.679	0.632	0.658	0.683
Sc	43.6	42.1	45.8	46.4	39.1	36.6	41.1	37.0	37.3	38.3	50.6
V	291	246	262	308	291	254	263	261	255	256	301
Cr	270	233	336	388	311	273	336	341	340	349	415
Co	41.7	34.3	41.6	47.8	42.3	37.5	42.1	42.2	43.1	42.6	52.3
Ni	82.8	65.7	88.4	98.8	84.3	78.7	102	96.6	109	96.4	135
Cu	74.4	67.3	74.4	87.3	73.7	65.9	77.7	78.7	77.8	77.5	95.6
Zn	88.7	74.7	77.1	91.8	86.4	76.1	78.7	82.7	78.0	78.3	91.3
Ga	8.95	7.97	10.7	12.6	11.8	10.4	11.0	13.7	13.5	13.3	15.7
Rb	0.797	0.667	1.07	1.24	1.72	1.53	1.49	1.40	1.36	0.958	0.948
Sr	130	126	136	154	153	141	145	135	134	131	158
Y	36.0	34.9	37.0	35.1	31.1	29.4	33.0	27.0	27.7	27.1	37.8
Zr	110	104	113	109	103	96.9	107	88.7	90.5	84.2	115
Nb	2.73	2.32	3.18	3.59	4.48	4.06	3.90	3.74	3.66	2.88	3.07
Cs	0.0186	0.0174	0.0260	0.0317	0.0343	0.0335	0.0308	0.0297	0.0313	0.0228	0.0245
Ba	7.07	6.28	9.72	11.3	17.7	15.8	13.6	12.8	12.4	8.78	8.75
La	3.46	3.16	3.78	4.05	4.38	4.11	4.12	3.69	3.72	3.21	3.88
Ce	11.0	9.39	10.3	12.1	13.3	11.7	11.5	10.9	10.6	9.68	11.1
Pr	1.90	1.69	1.83	2.06	2.12	1.92	1.93	1.78	1.74	1.64	1.96
Nd	10.1	9.32	9.84	10.7	10.6	9.75	10.0	8.84	8.85	8.38	10.5
Sm	3.56	3.29	3.48	3.61	3.53	3.24	3.37	2.99	3.00	2.89	3.68
Eu	1.26	1.17	1.21	1.32	1.26	1.15	1.20	1.09	1.07	1.06	1.30
Gd	5.02	4.95	5.15	5.19	4.70	4.38	4.89	3.90	4.01	3.89	5.36
Tb	0.869	0.864	0.905	0.884	0.788	0.751	0.826	0.677	0.691	0.686	0.931
Dy	5.76	5.68	5.93	5.80	5.19	4.94	5.59	4.39	4.49	4.42	6.06
Ho	1.24	1.23	1.28	1.25	1.12	1.03	1.18	0.921	0.960	0.930	1.30
Er	3.54	3.52	3.72	3.57	3.17	2.95	3.36	2.68	2.76	2.72	3.77
Yb	3.38	3.35	3.53	3.49	3.12	2.94	3.25	2.55	2.67	2.65	3.60
Lu	0.512	0.525	0.586	0.561	0.481	0.464	0.529	0.404	0.415	0.400	0.578
Hf	2.56	2.65	2.80	2.71	2.48	2.37	2.66	2.01	2.12	1.99	2.75
Ta	0.176	0.168	0.218	0.225	0.274	0.248	0.258	0.218	0.223	0.171	0.203
Pb	0.412	0.352	0.410	0.475	0.514	0.445	0.455	0.423	0.413	0.383	0.445
Th	0.128	0.127	0.195	0.202	0.245	0.220	0.245	0.196	0.203	0.148	0.171
U	0.0477	0.0416	0.0670	0.0791	0.0955	0.0803	0.0842	0.0733	0.0757	0.0579	0.0593

Table 3. (continued)

Sample	3963-3	3963-5	3963-6	3963-9	3963-10	4202-4	4202-6	4205-5	4205-6	2392-9 meas.	2392-9 accepted	Rel. Acc. (%)
Li	6.77	6.19	6.55	5.56	5.42	6.45	6.45	6.50	7.47	6.11		
Be	0.709	0.635	0.636	0.339	0.427	0.556	0.541	0.563	0.608	0.528		
Sc	44.7	46.9	44.7	38.9	36.1	39.8	40.6	41.4	43.0	39.4		
V	293	279	288	238	231	279	275	275	292	266		
Cr	315	310	310	325	360	277	283	286	288	361		
Co	42.1	39.9	41.9	45.3	43.8	43.1	42.5	41.1	42.6	45.8		
Ni	66.8	62.3	74.7	118	125	93.8	94.5	87.2	89.1	114	102	11.9%
Cu	76.2	74.7	79.6	86.0	85.0	77.4	77.3	75.9	77.3	84.1		
Zn	84.7	77.9	83.0	75.9	72.4	84.0	86.3	85.5	87.5	80.0		
Ga	13.8	13.4	13.7	13.5	13.5	9.36	9.39	9.20	9.79	13.8		
Rb	1.14	1.29	0.821	0.600	0.626	0.756	0.754	0.804	0.858	0.721	1.8	−59.9
Sr	135	135	136	125	132	121	124	124	131	132	124	6.3
Y	35.7	37.1	34.2	25.5	24.6	29.6	30.2	32.3	33.7	27.9	30.0	−7.1
Zr	109	112	103	71.9	73.6	87.2	88.8	95.3	101	82.9	90	−7.9
Nb	3.59	3.93	2.92	1.79	2.06	2.35	2.39	2.52	2.66	2.30	2.9	−20.6
Cs	0.0243	0.0286	0.0232	0.0192	0.0176	0.0191	0.0238	0.0264	0.0244	0.0224		
Ba	10.0	11.4	7.36	5.26	5.72	6.47	6.62	7.12	7.46	6.42	8.01	−19.9
La	3.95	4.14	3.64	2.40	2.60	2.92	3.01	3.22	3.40	2.88	3.0	−3.9
Ce	12.0	11.5	11.1	7.74	8.40	9.64	9.69	10.2	10.8	9.41	9.7	−3.0
Pr	2.01	1.97	1.91	1.35	1.45	1.65	1.68	1.75	1.87	1.60	1.6	0.2
Nd	10.7	10.6	10.2	7.35	7.61	8.73	8.87	9.37	9.94	8.58	8.24	−4.7
Sm	3.70	3.67	3.56	2.53	2.57	3.00	3.08	3.16	3.52	2.99	2.86	−0.2
Eu	1.33	1.30	1.28	0.98	1.02	1.13	1.17	1.20	1.27	1.10	1.1	0.3
Gd	5.26	5.41	5.24	3.71	3.71	4.19	4.37	4.66	5.02	4.13	4.2	−1.6
Tb	0.894	0.931	0.861	0.628	0.636	0.732	0.753	0.802	0.858	0.689	0.75	−8.1
Dy	6.04	6.27	5.89	4.27	4.25	4.89	5.15	5.40	5.77	4.69	4.8	−2.4
Ho	1.30	1.36	1.27	0.921	0.894	1.04	1.08	1.17	1.25	1.00	1.1	−9.3
Er	3.70	3.82	3.58	2.57	2.50	2.94	3.06	3.33	3.50	2.83	2.8	0.9
Yb	3.56	3.77	3.58	2.56	2.56	3.01	3.12	3.27	3.53	2.87	2.8	2.6
Lu	0.567	0.592	0.564	0.402	0.393	0.451	0.474	0.497	0.551	0.429	0.46	−6.7
Hf	2.75	2.92	2.67	1.75	1.84	2.13	2.25	2.41	2.62	2.02	2.2	−8.0
Ta	0.230	0.269	0.192	0.116	0.131	0.147	0.153	0.167	0.174	0.146		
Pb	0.472	0.445	0.449	0.326	0.362	0.380	0.398	0.420	0.447	0.403		
Th	0.204	0.248	0.172	0.093	0.110	0.115	0.126	0.145	0.151	0.119	0.1177	2.0
U	0.0702	0.0792	0.0659	0.0378	0.0455	0.0516	0.0502	0.0510	0.0594	0.0502	0.0478	4.6

[a]Trace element compositions were measured at Lamont-Doherty Earth Observatory (LDEO) using a New Wave UP 193 FX excimer laser ablation system coupled to a VG PlasmaQuad ExCell quadrupole ICP-MS. Laser operating conditions were as reported in *Cooper et al.* [2010], except all spot sizes were 100 μm. Concentrations were calculated after blank subtraction, correction to ^{49}Ti as an internal standard (using the TiO_2 electron probe data), and then calibrated with linear fits to USGS rock standards BIR-1, BHVO-2, and BCR-2, using values published by *Kelley et al.* [2003]. The reported concentrations are averages of two to three spots in glassy portions of each chip. External reproducibility was monitored with LDEO in-house MORB glass D7, with most elements determined better than 4% RSD (1σ) (exceptions are Ni, V, Th, Li, Cu, Cr, Co, and Pb, at 5–10% RSD; and U, Be, and Cs at 10–15% RSD). Accuracy is evaluated using repeated analyses of MORB standard ALV2392-9.

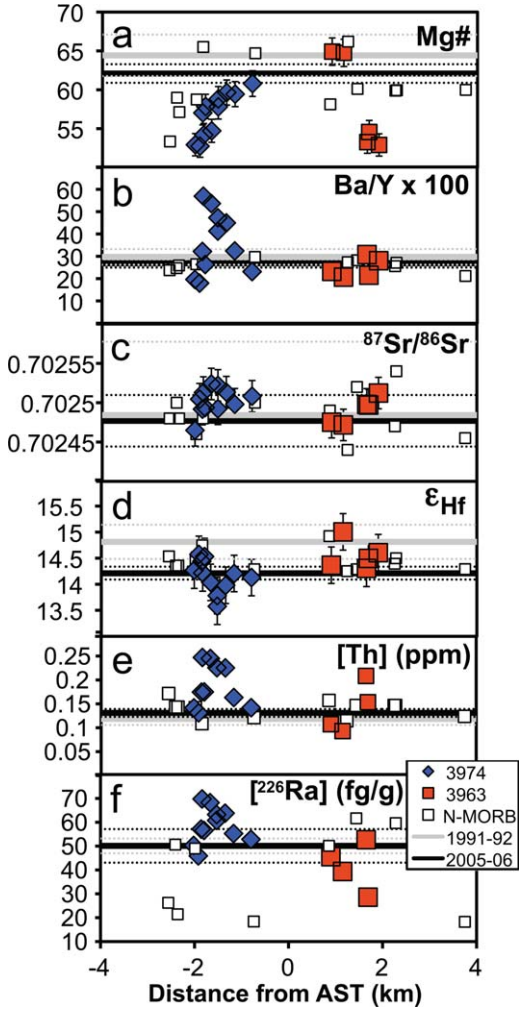

Figure 4. Distance from the axial summit trough versus (a) molar Mg# (Mg′/(Mg′+ 0.9Fe′) × 100), (b) Ba/Y × 100, (c) $^{87}Sr/^{86}Sr$, (d) ε_{Hf}, (e) Th (ppm), and (f) ^{226}Ra (fg/g) for dive 3974 and dive 3963 samples. The means (solid lines) and standard deviations (2σ; dashed lines) of sample populations interpreted to have erupted in 1991–1992 [*Rubin et al*., 1994; *Sims et al*., 2002] and 2005–2006 [*Goss et al*., 2010; this study] and collected from 9°48′ to 9°51.5′N EPR (Segment B1; *Haymon et al*. [1991]) are also shown. N-MORB lavas collected from up to ~4 km from the axial summit trough near 9°50′N EPR are shown for comparison [*Sims et al*., 2003].

footnotes. All measured dive 3963 and 3974 samples have $^{87}Sr/^{86}Sr = 0.702465–0.702570 \pm <20$ ppm (2σ), $^{143}Nd/^{144}Nd = 0.513135–0.513170 \pm <10$ ppm (2σ), and $^{176}Hf/^{177}Hf = 0.283156–0.283196 \pm <10$ ppm (2σ). Samples 3974-5, 6, 7, 8, and 9 and 3963-5 have Nd and/or Hf isotope compositions that are more enriched than previously measured N-MORB lavas from 9 to 10°N EPR. All other samples have Sr, Nd, and Hf isotope compositions that are indistinguishable from previously measured N-MORB lavas from 9 to 10°N EPR [*Goss et al*., 2010; *Sims et al*., 2002, 2003; *Waters et al*., 2011] (Figures 4c, 4d, and 5). In addition, $^{87}Sr/^{86}Sr$, $^{143}Nd/^{144}Nd$, and $^{176}Hf/^{177}Hf$ compositions track with each other as well as other measures of enrichment (due to either variations in source composition or the degree of melting), such as incompatible element abundances and ratios such as Th, ^{226}Ra, K/Ti, Ba/Y, and Th/U (Figure 4), and they trend towards E-MORB compositions from 9°N to 10°N EPR (Figure 5) [*Waters et al*., 2011].

3.3. U-series Isotopes

[16] ^{238}U-^{230}Th-^{226}Ra, ($^{230}Th/^{232}Th$), and ($^{234}U/^{238}U$) isotopic compositions and U, Th and ^{226}Ra abundances, as measured by ID, are reported in Table 5 along with the details of the analytical methods. All the measured samples have ($^{234}U/^{238}U$) in equilibrium within analytical uncertainties (1.000± 5‰) indicating that these samples have not undergone secondary alteration due to seawater-rock interaction following eruption. For submarine basalts, ($^{234}U/^{238}U$) is a sensitive indicator of alteration, as seawater is significantly enriched in ^{234}U relative to ^{238}U (for seawater, $(^{234}U/^{238}U) = 1.14 \pm 0.03$) [*Henderson et al*., 1993; *Ku et al*., 1977; *Robinson et al*., 2004; *Thurber*, 1962]. Thus, the U-series compositions we observe can be attributed to magmatic processes.

[17] Though limited in quantity and geographic coverage, the suite of 2005–2006 eruption samples that we measured are indistinguishable from lavas collected from the 1991–1992 eruption with respect to ($^{230}Th/^{232}Th$) (1.383–1.398) and ^{230}Th excesses (1.108–1.122), but are more homogeneous (Figure 6a). Samples from the 2005–2006 eruption have ^{226}Ra excesses ranging from 2.41 to 2.56 (Table 5, Figure 6b). Compared to previous ^{226}Ra data obtained on samples from the axial summit trough, these samples have slightly lower ($^{226}Ra/^{230}Th$) at a given ($^{230}Th/^{238}U$) (Figure 6b).

[18] We observe three key features in the U-series data set for dives 3974 and 3963:

(1) All dive 3974 and 3963 samples have significant ^{226}Ra excesses (($^{226}Ra/^{230}Th$)>1; 1.21–2.73; Figure 6b; Table 5) and trend to lower values than previously measured axial samples (2.01–2.89) [*Rubin et al*., 2005; *Sims et al*., 2002]. The presence of ^{226}Ra excesses

Table 4. $^{87}Sr/^{86}Sr$, $^{143}Nd/^{144}Nd$, and $^{176}Hf/^{177}Hf$ isotopic compositions of Dive 3963, Dive 3974, and 2005–2006 lavas collected from 9°50′N EPR[a]

Sample	$^{87}Sr/^{86}Sr$	$\pm 2\sigma$ (ppm)	$^{143}Nd/^{144}Nd$	$\pm 2\sigma$ (ppm)	ε_{Nd}	$^{176}Hf/^{177}Hf$	$\pm 2\sigma$ (ppm)	ε_{Hf}
3974-1	0.702653[b]		0.513152	4	10.03	0.283176	5	14.27
	0.702465[c]	8						
3974-2	0.702566[b]		0.513162	5	10.22	0.283184	4	14.57
	0.702504[c]	10						
3974-3	0.702580[b]		0.513144	5	9.88	0.283183	4	14.53
	0.702494[c]	9						
3974-4	0.702635[b]		0.513152	5	10.02	0.283180	5	14.44
	0.702492[c]	7						
3974-5	0.702610[b]		0.513139	5	9.77	0.283174	6	14.22
	0.702513[c]	7						
3974-6	0.702577[b]		0.513138	4	9.75	0.283169	7	14.04
	0.702524[c]	11						
3974-7	0.702581[b]		0.513144	4	9.86	0.283162	4	13.78
	0.702492[c]	9						
3974-8	0.702522[b]		0.513135	4	9.69	0.283156	4	13.58
	0.702570[c]	8						
3974-9	0.702592[b]		0.513137	5	9.72	0.283167	4	13.98
	0.702513[d]	20						
3974-10	0.702498[b]		0.513149	4	9.97	0.283174	4	14.21
	0.702569[c]	9						
3974-11	0.702536[b]		0.513151	4	10.01	0.283172	4	14.13
	0.702508[c]	13						
3963-3	0.702512[c]	9	0.513156	4	10.10	0.283185	6	14.61
3963-5	0.702498[c]	7	0.513146	4	9.90	0.283177	6	14.30
3963-6	0.702497[c]	10	0.513153	4	10.05	0.283182	4	14.50
3963-9	0.702472[c]	9	0.513170	5	10.38	0.283196	5	15.01
3963-10	0.702475[c]	7	0.513151	4	10.00	0.283178	5	14.36
4202-4			0.513159	5	10.16	0.283174	3	14.21
4202-6			0.513161	4	10.20	0.283176	3	14.27
4205-5			0.513150	4	9.99	0.283172	3	14.13
4205-6			0.513152	4	10.03	0.283175	3	14.24

[a]Sr isotopic analyses were conducted both at Woods Hole Oceanographic Institution (WHOI) using a Thermo Finnigan Neptune multicollector inductively coupled plasma mass spectrometer (MC-ICP-MS) and at Boston University (BU) using the Thermo Finnigan Triton thermal ionization mass spectrometer (TIMS). Measurements of Sr isotopic compositions have internal precision of 5–10 ppm (2σ) (WHOI); internal precision for measurements at BU is reported for each sample. After adjusting to 0.710240 (NBS SRM 987), external precision for both measurements made at WHOI and BU is estimated at 15–30 ppm. The Sr whole chemistry blank is estimated at 500–600 pg. Neodymium and hafnium were separated from the same acid attacks of hand-picked MORB glasses at the Ecole Normale Supérieure (ENS) in Lyon, and their isotopic compositions measured using a Nu Plasma HR MC-ICP-MS coupled with a desolvating nebulizer Nu DSN-100, likewise at ENS Lyon. The chemical separation procedures and mass spectrometric protocols followed are given in *Blichert-Toft et al*. [1997], *Blichert-Toft* [2001], *Blichert-Toft et al*. [2005], and *Blichert-Toft and Albarède* [2009]. Measured Nd and Hf isotopic ratios were normalized for instrumental mass fractionation relative to, respectively, $^{146}Nd/^{144}Nd = 0.7219$ and $^{179}Hf/^{177}Hf = 0.7325$ using an exponential law. Accuracy and external analytical uncertainties of $< \pm 30$ ppm for both Nd and Hf isotopic measurements were estimated from repeated runs of the "Rennes" in-house Nd standard [*Chauvel and Blichert-Toft*, 2001] and the JMC-475 Hf standard [*Blichert-Toft et al*., 1997], which gave, respectively, 0.51196 ± 0.00001 (2σ) and 0.28216 ± 0.00001 (2σ) for $^{143}Nd/^{144}Nd$ and $^{176}Hf/^{177}Hf$ during the course of this study. In-run analytical errors were half that for both elements. Nd and Hf total procedural blanks were <20 pg. ε_{Nd} and ε_{Hf} values were calculated using $(^{143}Nd/^{144}Nd)_{CHUR(0)} = 0.512638$ and $(^{179}Hf/^{177}Hf)_{CHUR(0)} = 0.282772$ [*Blichert-Toft and Albarède*, 1997].

[b]Sr isotopic composition measured at WHOI by Thermo Finnigan Neptune MC-ICP-MS; glass was not leached.

[c]Sr isotopic composition measured at BU by Thermo Finnigan Triton TIMS; glass was leached; ~100 ng of Sr was loaded onto a Re single filament.

[d]Sr isotopic composition measured at Boston University by Thermo Finnigan Triton TIMS; glass was leached; ~10 ng Sr was loaded onto the filament.

indicates that all dive 3974 and 3963 lavas must have erupted within the last ~8 ka.

(2) As a whole, samples collected during dive 3974 have significantly variable U and Th concentrations (U = 0.056–0.096 ppm, Th = 0.131–0.247 ppm), but discrete subgroups, consisting of spatially related samples from geologically continuous flow units, have U and Th concentrations that are indistinguishable within analytical uncertainties (Table 5). These sample groupings are one of the most striking features of this data set, and although best observed in U and Th ID concentration data, they are also generally consistent throughout the U-series [^{226}Ra concentrations, ($^{230}Th/^{232}Th$), ($^{230}Th/^{238}U$), and ($^{226}Ra/^{230}Th$) (Table 5)] and major and trace element data sets.

(3) Samples collected in the middle of the dive 3974 transect, namely 3974-5, 6, 7, 8, and 9, as well as sample 3963-5, have more enriched compositions. Namely, they have higher U (0.079–0.091 ppm), Th (0.208–0.247 ppm), and ^{226}Ra (52.7–69.8 fg/g) abundances, higher

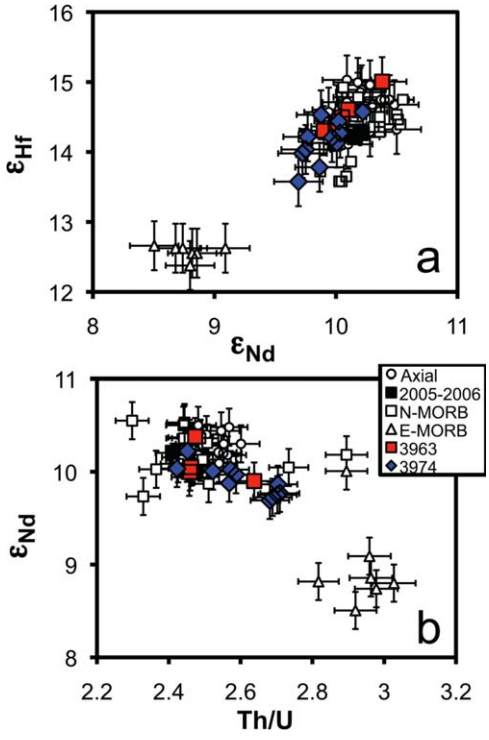

Figure 5. Variations in (a) ε_{Nd} versus ε_{Hf} and (b) Th/U (as measured by ID) versus ε_{Nd} for dive 3974, dive 3963, and 2005–2006 eruption samples. Samples collected from within the axial summit trough [*Sims et al*., 2002] and other N-MORB collected up to ~4 km away from the axial summit trough [*Sims et al*., 2003] from 9°48′ to 9°53′N EPR are shown for comparison, as are N-MORB and E-MORB collected from outside of the neo-volcanic zone at 9°30′N–9°35′N EPR and 9°53′N EPR [*Waters et al*., 2011]. Dive 3974 samples, in particular, trend towards E-MORB compositions.

Th/U (2.64–2.70), and lower (^{230}Th/^{232}Th) (1.30–1.34) and (^{226}Ra/^{230}Th) (1.69–1.96) than typical N-MORB samples collected from 9 to 10°N EPR (e.g., 1991–1992 samples average U ~0.054 ppm, Th ~0.137 ppm, ^{226}Ra ~50.5 fg/g, Th/U ~2.51, (^{230}Th/^{232}Th) ~1.39, and (^{226}Ra/^{230}Th) ~2.46; *Rubin et al*. [2005]; *Sims et al*. [2002]) (Figures 4 and 6). These enrichments in U, Th, and ^{226}Ra abundances, Th/U, (^{230}Th/^{232}Th), and (^{226}Ra/^{230}Th) also correspond to significant enrichments in other incompatible trace elements, incompatible trace element ratios (e.g., Ba/Y and La/Sm), and Sr, Nd, and Hf isotope compositions (Figures 4 and 5).

[19] All other dive 3974 and 3963 samples have U, Th, and ^{226}Ra abundances, (^{230}Th/^{232}Th), ^{230}Th excesses (i.e., (^{230}Th/^{238}U)>1), and ^{226}Ra excesses (i.e., (^{226}Ra/^{230}Th)>1) similar to previously measured N-MORB from 9°50′N EPR [*Goldstein et al*., 1993, 1994; *Lundstrom et al*., 1999; *Rubin et al*., 2005; *Sims et al*., 2002, 2003; *Waters et al*., 2011]. In addition, consistent with previous studies of young lavas from 9°50′N EPR, ^{230}Th excesses are negatively correlated with ^{226}Ra excesses (Figure 6b), and (^{230}Th/^{232}Th) is positively correlated with (^{238}U/^{232}Th) (Figure 6a) and negatively correlated with U and Th elemental abundances for dive 3974 and 3963 samples [*Goldstein et al*., 1993, 1994; *Lundstrom et al*., 1999; *Sims et al*., 2002, 2003; *Waters et al*., 2011]. The only exception to this is sample 3963-6, which has lower (^{226}Ra/^{230}Th) = 1.21 that does not correlate with ^{230}Th excesses; this lower (^{226}Ra/^{230}Th) is most likely due to posteruption aging.

4. Discussion

4.1. Age Determinations

[20] We evaluated the use of a ^{230}Th-^{226}Ra model age method adapted from *Sims et al*. [2003] for resolving lava ages in dives 3974 and 3963. We used a maximum likelihood, double-error regression to fit a zero-age trend line [*Sohn and Menke*, 2002] to a data set including previous data obtained on samples collected within the axial summit trough from 9°37′–9°54′N EPR [*Sims et al*., 2002] and data obtained in this study for samples collected from flows associated with the 2005–2006 eruption (Figure 6b). Many of the samples collected from the axial summit trough from 9°37′N to 9°54′N are interpreted to have erupted during the 1991–1992 eruption and include several samples whose eruption ages have been constrained to the 1991–1992 eruption by ^{210}Po-^{210}Pb dating [*Rubin et al*., 1994]. The equation for this line is (^{226}Ra/^{230}Th) = −17.71283 × (^{230}Th/^{238}U) + 22.66071, $r = -0.665$, mean square of the weighted deviates (MSWD) = 10.051. Confidence limits (95%) for the zero-age trend lines were estimated using bootstrap methods (1000 replicates) for the slope (−27.37< −17.71<−12.10) and intercept (16.11<22.66 <33.47) and take into account measurement uncertainties on both (^{230}Th/^{238}U) and (^{226}Ra/^{230}Th). We note that this trend has previously been interpreted as a mixing trend [*Sims et al*., 2002, 2003] and since the denominators for the X and Y axes are not equivalent, we should expect mixing to be best approximated by a hyperbola. However, fitting a hyperbola to these data requires confidence in our knowledge of the end member mixing components [*Sohn*, 2005], but these are poorly constrained by only few samples

with known initial ($^{226}Ra/^{230}Th$) [cf., *Elkins*, 2009; *Lundstrom et al*., 1999; *Sims et al*., 2002; *Waters et al*., 2011]. Thus, we approximate the mixing trend with a line, noting that fitting a binary mixing curve through these "zero-age" data [*Sohn*, 2005] using two (X, Y) coordinates calculated from the line fit for end member ratios results in a curvature of 0.967 ± 0.07. This value is within error of 1, the case for a straight line, providing support that our approximation of linearity is justified.

[21] Because there is scatter about this zero-age ($^{230}Th/^{238}U$)-($^{226}Ra/^{230}Th$) trend line, and thus uncertainty in the estimate of initial U-series disequilibria, we applied a statistical treatment to the data set to determine how well lava ages could be resolved from this trend line. We then performed an outlier test to determine if any of the dive 3974 and 3963 samples fall outside of the zero-age trend line confidence intervals. We accomplished this by calculating the Studentized residual for each sample from dive 3974 and 3963 to the zero-age trend line and comparing this value to a critical value for outliers (based on the Bonferroni inequality) at the 95% confidence level [*Sohn and Menke*, 2002]. Using this method, only sample 3963-6 (($^{226}Ra/^{230}Th$) ~1.21) was identified as an outlier at the 95% confidence interval. Thus, zero-age lavas display enough scatter about the zero-age trend line such that only one sample from dives 3974 and 3963 samples can be unequivocally identified as belonging to a distinct population in both ($^{230}Th/^{238}U$) and ($^{226}Ra/^{230}Th$) from the zero-age trend. Based on our statistical analysis, we find that all dive 3974 and 3963 samples are <2.2 ka at the 95% confidence level with the exception of sample 3963-6, which has a ^{230}Th-^{226}Ra model age of ~5 ka. Both this sample's greater sediment cover relative to the other dive samples in dive photographs (Figure 3) and its higher than present-day magnetic paleointensity of ~44.5 μT are consistent with this interpretation [*Bowles et al*., 2006].

[22] With the exception of sample 3963-6, we are unable to resolve age differences among samples from dives 3974 and 3963, and consequently, within the neo-volcanic zone at 9°50′N EPR, we cannot confidently use ^{230}Th-^{226}Ra model ages to classify samples into temporally distinct eruptive units, nor can we determine stratigraphic relationships among lava flows. We can, however, conclude that the bulk of the neo-volcanic zone at 9°50′N EPR is represented by lava flows younger than ~2 ka. Given our current understanding of the variability in U-series disequilibria in zero-age lavas, coupling ^{230}Th-^{226}Ra methods with magnetic paleointensity dating methods may prove useful, though paleointensity methods suffer different limitations, such as the inherent nonuniqueness of the paleointensity record and cooling bias [e.g., *Bowles et al*., 2006; *Carlut et al*., 2004]. (For example, we attempted to analyze several dive 3974 samples for magnetic paleointensities; however, samples did not have enough glass chips with sufficient natural remanent magnetization to allow for useful paleointensity measurements). Age constraints obtained using ^{226}Ra-^{210}Pb disequilibria, which we did not measure in this study, would be useful for identifying lavas erupted within the past 100 years [cf., *Bergmanis et al*., 2007].

4.2. Combining Geological, Geochemical, and Age Relationships Among Samples

[23] Because ^{230}Th-^{226}Ra model ages are inadequate for resolving the relatively small age differences represented by dive 3974 and dive 3963 samples, we also attempt to understand lava stratigraphy using geochemistry. In Figure 7, we show the coefficient of variability, (S_i, % 2σ), the analytical precision (P_i, % 2σ), and the corresponding precision-normalized variability (S_i/P_i, 2σ) for select geochemical indices, i (e.g., element concentration or isotope ratio), for dive 3974 samples. The details of the estimates of analytical precision for dive 3974 samples are given in the footnotes to Tables 2–5. From Figure 7, we can see that Th and U concentrations, as measured by ID, have the greatest precision-normalized variability (variability is ~25–30 × analytical uncertainty) and are thus our most reliable metrics for subdividing the sample population into geochemically distinct groups. Thus, we interpret the preliminary groupings we identified above in results section 3.3 based on sample Th and U ID concentrations for dive 3974 and 3963 samples as having geological meaning. These groups also have similar major element, incompatible element, and long-lived radiogenic isotope compositions. However, it is important to note that groupings using major element, incompatible element, and long-lived radiogenic isotope compositions are not always as clearly defined as those using Th and U ID concentrations due to their lower precision-normalized variability, and thus more compositional overlap among groups is apparent.

[24] Based on our geochemical observations, we group together samples 3974-3 and 3974-4 (Th=0.175 ppm, Mg#~57–58, K_2O/TiO_2 ×

Table 5. (^{230}Th/^{232}Th), (^{230}Th/^{238}U), (^{226}Ra/^{230}Th), (^{234}U/^{238}U), and U, Th, and Ra Concentrations Measured by MC-ICP-MS and Single-Collector ICP-MS for Dive 3963, Dive 3974, and 2005–2006 Lavas Collected from 9°50′N EPR[a]

Sample	[Th] (ppm)[a,b]	[U] (ppm)[a,b]	Th/U[a]	(^{238}U/^{232}Th)[a,d]	(^{230}Th/^{232}Th)[e]	(^{234}U/^{238}U)[f]	(^{230}Th/^{238}U)	[^{226}Ra] (fg/g)[g]	(^{226}Ra/^{230}Th)
3974-1	0.1418	0.0583	2.433	1.247	1.437	1.001	1.148	50.29	2.217
	0.1416	0.0585	2.423	1.252	1.431		1.140		
3974-2	0.1311	0.0536	2.445	1.241	1.401	0.999	1.130	45.91	2.238
	0.1314	0.0537	2.452	1.237					
3974-3	**0.1760**	**0.0686**	**2.565**	**1.183**	**1.340**	**1.001**	**1.132**	**56.56**	**2.176**
	0.1740	**0.0679**	**2.568**	**1.181**					
3974-4	**0.1753**	**0.0686**	**2.555**	**1.187**	**1.343**	**0.999**	**1.136**	**57.14**	**2.197**
	0.1738	**0.0677**	**2.572**	**1.179**					
3974-5	0.2472	0.0916	2.700	1.124	1.314	1.000	1.171	69.76	1.930
	0.2468	0.0913	2.709	1.120					
3974-6	0.2454	0.0907	2.704	1.122	1.309	1.001	1.164	68.22	1.913
	0.2444	0.0906	2.703	1.123					
3974-7	**0.2250**	**0.0840**	**2.678**	**1.133**	**1.305**	**1.003**	**1.161**	**63.23**	**1.921**
	0.2263	**0.0839**	**2.704**	**1.122**					
3974-8	**0.2257**	**0.0842**	**2.681**	**1.132**	**1.300**	**1.002**	**1.147**	**60.75**	**1.859**
	0.2255	**0.0842**	**2.682**	**1.131**					
3974-9	**0.2253**	**0.0841**	**2.681**	**1.132**	**1.297**	**1.003**	**1.147**	**63.81**	**1.960**
	0.2253	**0.0839**	**2.689**	**1.128**					
3974-10	0.1629	0.0638	2.553	1.188	1.352	1.004	1.150	55.27	2.240
	0.1638	0.0634	2.587	1.173					
3974-11	0.1420	0.0564	2.523	1.203	1.371	1.003	1.138	52.83	2.435
3963-5	0.2084	0.0790	2.638	1.150	1.342	1.004	1.165	52.69	1.693
3963-6	0.1535	0.0623	2.462	1.232	1.385	1.003	1.122	28.59	1.209
3963-9	0.0931	0.0377	2.474	1.226	1.394	1.003	1.134	39.36	2.726
3963-10	0.1075	0.0437	2.459	1.234	1.410	1.001	1.141	45.56	2.704
4202-4	0.1249	0.0515	2.430	1.249	1.398	1.000	1.118	46.72	2.405
4202-4[d]	0.1253	0.0519	2.413	1.257					
4202-4[i]	0.1261	0.0519	2.429	1.249	1.387	1.003			
4202-4[i]		0.0509				0.997	1.110		
4202-6	0.1233	0.0512	2.412	1.258	1.396	1.001	1.108	47.44	2.478
4202-6[d]	0.1232	0.0509	2.421	1.260		1.000			
4202-6[i]	0.1469	0.0589	2.495	1.216	1.353	1.003	1.112		
4202-6[i]	0.1480	0.0592	2.499	1.217					
4205-5	0.1362	0.0553	2.467	1.230	1.383	1.002	1.122	53.57	2.555
4205-5[d]	0.1364	0.0557	2.449	1.239					
4205-5[i]	0.1393	0.0558	2.496	1.217	1.396	1.004	1.148		
4205-6	0.1335	0.0547	2.448	1.239	1.390	1.002	1.120	52.67	2.550
4205-6[d]	0.1344	0.0549	2.446	1.239					
4205-6[d]	0.1343	0.0549	2.449	1.240		0.993			
4205-6[i]	0.1285	0.0526	2.443	1.248	1.385	1.001	1.114		
4205-6[i]		0.0521							
2392-9[i]	0.1160	0.0476	2.436	1.246	1.402	1.005	1.125		
Standards									
TML/3[b]	30.384	10.819	2.814	1.078	1.082	1.002	1.002	3,669	1.011
	30.625	10.775	2.842	1.067	1.083		1.002	3,675	1.009
					1.081		1.000	3,709	1.018
					1.073		0.993	3,698	1.015
					1.074		0.994		
TML8R[i]	29.892	10.558	2.831	1.072	1.072	1.000	0.997		
AThO/3	7.5223	2.2642	3.322	0.913	1.017	1.001	1.114	861.4	1.006
					1.028		1.124	834.6	0.975

^{238}U, ^{232}Th, ^{226}Ra, (^{230}Th/^{232}Th), and (^{234}U/^{238}U) were measured at WHOI using the Thermo Finnigan Neptune MC-ICP-MS. Extensive details of the U-Th-Ra chemical and analytical procedures at WHOI are presented in Appendix A1 of *Sims et al*. [2008a]. More details of Th and U isotope measurement methods and standards are summarized in *Ball et al*. [2008] and *Sims et al*. [2008b]. Values for two sets of samples with indistinguishable U and Th abundances are shown in boldface to highlight the groupings as discussed in the text.

[a]Duplicate measurements represent spiking and purification of U and Th for separate samples of the same glass dissolution. In the laboratory, the samples were hand-picked under a microscope, then ultrasonically leached in sequential treatments of 0.1N HCl plus 2% H_2O_2 (15 min), DI water (twice, each time for 15 min), 0.1N oxalic acid plus 2% H_2O_2, and DI water (twice, each time for 15 min). Samples were then hand-picked by microscope for a second time to assure clean glass devoid of visual alteration. Sample splits (~2–3 g) were then dissolved, aliquotted, spiked and then U, Th, and Ra were separated using chemical techniques outlined in *Sims et al*. [2008a, 2008b].

[b]~400 mg of sample powder was dissolved for TML/3.

[c][U] and [Th] were measured by ID-ICP-MS using the Thermo Finnigan Element 2 (analyst C. Waters). Measurement reproducibility (2σ) for [U] and [Th] ranges from 1.4% to 2.1% (mean=1.5%) and 1.2%–2.5% (mean=1.5%), respectively.

[d]() denotes activity $\lambda_{238} = 1.551 \times 10^{-10}$ yr^{-1}; $\lambda_{232} = 4.948 \times 10^{-11}$ yr^{-1}; (^{238}U/^{232}Th) errors (2σ) range from 1.9% to 2.9% and do not include uncertainties in λ_{238} (0.07%) or λ_{232} (0.5%).

[e]Th isotopic compositions measured by Thermo Finnigan Neptune MC-ICP-MS at WHOI [*Ball et al*., 2008; *Sims et al*., 2008b]; activity ratios calculated using $\lambda_{230} = 9.195 \times 10^{-6}$ yr^{-1} and $\lambda_{232} = 4.948 \times 10^{-11}$ yr^{-1}; errors (2σ) range from 0.7% to 1.6% and do not include uncertainties in λ_{230} (0.4%) or λ_{232} (0.5%).

[f](^{234}U/^{238}U) measured by Thermo Finnigan Neptune MC-ICP-MS at WHOI; $\lambda_{234} = 2.823 \times 10^{-6}$ yr^{-1}, errors (2σ) < 0.6%; for these samples (^{234}U/^{238}U) = 1 within error, using an equilibrium (^{234}U/^{238}U) of 54.48 ppm for U010 [*Richter and Goldberg*, 2003]. NBS 960 was first bracketed by standard U010 to cross-calibrate U010. U010 was then used as a bracketing standard for all sample measurements to determine mass bias.

[g](^{226}Ra) measured by ID using the Thermo Finnigan Neptune MC-ICP-MS at WHOI after *Sims et al*. [2008a]; $\lambda_{226} = 4.331 \times 10^{-4}$ yr^{-1}; measurement errors (2σ) range from 3.2% to 6.5% and do not include uncertainties in λ_{226} (0.4%) or λ_{230}. For all samples accuracy is limited by uncertainties (2σ; 1.5%) on the NBS ^{226}Ra standard used to calibrate the ^{228}Ra spike.

[h]Replicate [U] and [Th] abundances for the 2005–2006 eruption samples were measured by ID-ICP-MS using a Thermo Fisher Neptune Plus MC-ICP-MS on separate dissolutions of ~100 mg of each sample at the University of Wyoming (WILD; analysts K. Sims and Erin Philips-Writer). Replicate values for sample 4205-6 are machine replicates on a single aliquot of the same spiked and purified solution. Although the University of Wyoming data agree with the WHOI data to better than 1%, analytical reproducibility is estimated at >1% (2σ), as the spike concentrations cannot be known to better than the 1.4% and 1.2% uncertainties in the U and Th standards against which they are calibrated.

[i][U] and [Th] abundances, ^{230}Th/^{232}Th, and ^{234}U/^{238}U measured by Thermo Finnigan Neptune MC-ICP-MS at the University of Bristol (Bristol Isotope Group, BIG, analyst J. Prytulak) using measurement protocols described by *Hoffmann et al*. [2007] and *Sims et al*. [2008b]. Analytical uncertainties were calculated using a Monte Carlo propagation scheme as described in *Hoffmann et al*. [2007] and are as follows: U<0.3% (2σ), Th<0.5% (2σ), (^{230}Th/^{232}Th)<1.6% (2σ), and (^{234}U/^{238}U)<0.2% (2σ).

100~8.7–9.0, ε_{Hf}~14.4–14.5), samples 3974-5 and 3974-6 (Th=0.245–0.247 ppm, Mg#~54–55, $K_2O/TiO_2 \times 100$~10.2–10.6, ε_{Hf}~14.0–14.2), and samples 3974-7, 3974-8, and 3974-9 (Th=0.225 ppm, Mg#~58–60, $K_2O/TiO_2 \times 100$~10.0–10.5, ε_{Hf}~13.6–14.0). We also can group samples 3963-9 and 3963-10 (Th=0.123–0.125 ppm, Mg#~65, $K_2O/TiO_2 \times 100$~7.2–8.2, ε_{Hf}~14.4–15.0). These groupings are generally consistent with spatial and geological observations (Table 1; Figures 2 and 3): (1) samples 3974-3 and 3974-4 were collected from the same body of mixed sheet and lobate flows; (2) samples 3974-5 and 3974-6 were collected in close proximity to each other from the same pillow flow that is observably distinct from 3974-3 and 3974-4; (3) sample 3974-7 was collected from a sheet flow breakout at the basal end of the pillow front from which 3974-8 was collected, and 3974-9 was collected from the lobate flow body of the same unit further upslope; and, (4) although sample 3963-10 was collected from a pillow flow front upslope from 3963-9 (Figure 3), it is likely that the channel from which 3963-9 was sampled was fed from the same flow as 3963-10.

[25] We infer that these groups represent individual magma batches, with the caveat that single eruptive episodes may sample multiple magma batches [e.g., *Maclennan et al*., 2003]; thus, these groupings do not necessarily represent individual eruptions. We think that it is unlikely that these groupings include samples from successive individual eruptions because three of these "magma batches" with distinct Th and U ID compositions were collected within geologically defined flow units, and either 1991–1992 or 2005–2006 eruptions exhibit more geochemical variability alone than any of these groups [*Goss et al*., 2010; *Sims et al*., 2002].

[26] Other samples are not as easily distinguished by geographic, geological, geochemical, isotopic, or age characteristics. Sample 3974-1 was collected west of the first flow front from which sample 3974-2 was collected. These two samples have distinct Th and U abundances, but compositions (Th=0.131–0.142 ppm, Mg#~53, $K_2O/TiO_2 \times 100$~6.6–6.8, ε_{Hf}~14.3–14.6) that are otherwise more similar to each other than to grouped samples 3974-3 and 3974-4. Sample 3974-10 was sampled from a pillow flow front just upslope of sample 3974-9 and is compositionally distinct from it (Th=0.163 ppm, Mg#~59, $K_2O/TiO_2 \times 100$~8.4, ε_{Hf}~14.2). Sample 3974-11 (Th=0.142 ppm, Mg#~61, $K_2O/TiO_2 \times 100$~8.4, ε_{Hf}~14.1) was collected from the flat area ~700 m west of the axial summit trough and also has distinct Th and U abundances compared to 3974-10.

[27] On the east side of the axial summit trough, dive 3963 geological relationships are more easily discerned, as the slope is shallower (~35 m/km) compared to the west side of the axial summit trough (~70 m/km), and the shingle-patterned terrain is better defined (Figure 3). For example, sample 3963-6 is older than sample 3963-5, which was collected from the pillow flow front immediately upslope. The older sample 3963-6 also has a more depleted composition (Th=0.154 ppm, Mg#~55, $K_2O/TiO_2 \times 100$~8.6, ε_{Hf}~14.5) than sample 3963-5 (Th=0.208 ppm, Mg#~53, $K_2O/TiO_2 \times 100$~10.8, ε_{Hf}~14.3). Samples 3963-9 and 3963-10 were collected from much closer to the axis and have similar primitive, incompatible element depleted compositions.

[28] We can further compare the geochemical diversity among these groups to the diversity that can be attributed to a single eruption (i.e., the 1991–1992 and 2005–2006 eruptions; Figures 4, 8, and 9). Dive 3974 and 3963 sample Th and U

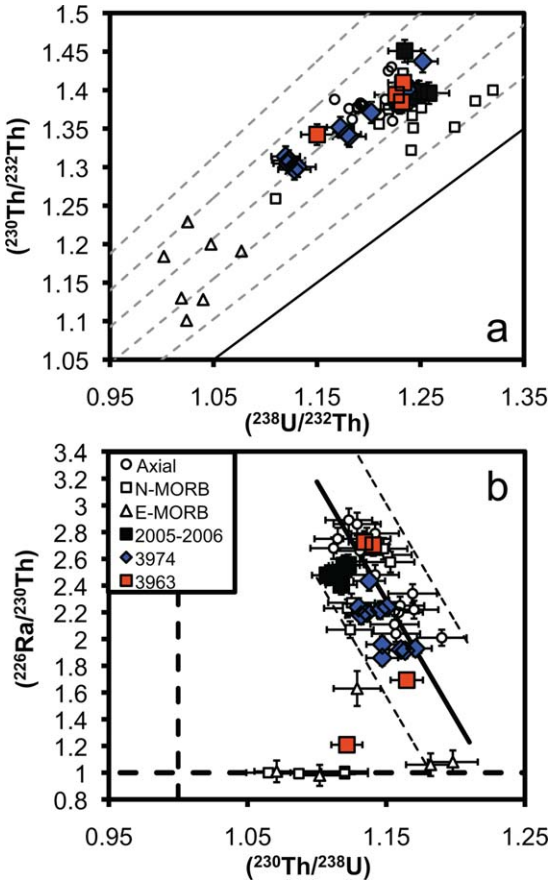

Figure 6. **(a)** Equiline diagram comparing (^{238}U/^{232}Th) with (^{230}Th/^{232}Th) among samples collected from within the axial summit trough from 9°17′N to 9°54′N, including samples from the 1991–1992 eruption [*Sims et al*., 2002]; samples collected from up to ~4 km away from the axial summit trough at 9°50′N [*Sims et al*., 2003]; E-MORB and N-MORB collected from up to ~5 km east of the axial summit trough at 9°30′–9°35′N and outside of the neo-volcanic zone at 9°53′N [*Waters et al*., 2011]; samples from dive 3974 on the west side of the ridge crest at 9°50′N; samples from dive 3963 on the east side of the ridge crest at 9°50′N; and, samples collected from the 2005–2006 eruption. **(b)** (^{230}Th/^{238}U) versus (^{226}Ra/^{230}Th) showing the zero-age trend line calculated from a double-error, maximum likelihood, non-linear least squares fit for a line [*Sohn and Menke*, 2002] to both data obtained on samples collected within the axial summit trough north of 9°37′N EPR [*Sims et al*., 2002] and data obtained in this study for samples collected from flows associated with the 2005–2006 eruption (see text for details). The dashed lines that are parallel to the trend line are the 95% confidence limits for the "zero-age" population. All but one sample plot within the 95% confidence limits and follow the trend line. Also shown for comparison are samples collected away from the axial summit trough at 9°50′N and previously dated with the ^{230}Th-^{226}Ra model age technique [*Sims et al*., 2003].

ID abundances are ~4–5 times more variable than Th and U ID data for 1991–1992 eruption samples from the 9°50′N region and may be useful for distinguishing eruptive units (e.g., Figure 4e). Because the geochemical compositions of 1991–1992 and 2005–2006 lavas from the fourth-order segments north and south of Segment B1 (bounded by 9°49′N and 9°51.5′N) are more heterogeneous than those collected from within Segment B1 owing to discontinuities in the underlying axial magma chamber and along-axis variations in magma differentiation processes [cf., *Goss et al*., 2010; *Haymon et al*., 1991; *Rubin et al*., 1994], we compare our samples to Segment B1 lavas (Figure 8) [*Goss et al*., 2010; *Rubin et al*., 2005; *Sims et al*., 2002], assuming that the fourth-order segmentation and robust axial magma chamber have remained persistent for the last few thousand years. If, instead, magma chamber characteristics that influence the extent of mixing and melt zoning (e.g., crystallinity, melt supply) have varied substantially during the relatively short time interval over which dive 3974 and 3963 lavas were erupted, then this type of comparison will underestimate the potential geochemical diversity in a single eruption, and therefore overestimate the number of eruptions these samples represent.

[29] Here we discuss three possible eruption scenarios, noting that it is impossible to determine the true eruption sequence represented by dives 3974 and 3963 with certainty without knowing "exact" sample ages, more thorough geological surveying and sampling of individual shingles and flow features, and/or a more comprehensive, longer record of intra- versus inter-eruption geochemical variability at 9°50′N EPR. That being said, these flows and samples are among the most well characterized on any MOR.

[30] (1) *Single, heterogeneous eruption*. All dive 3974 and 3963 samples (barring 3963-6) could be due to a single eruption. Such an eruption would be expected to tap a large body of magma, as lava would reach up to ~2 km on either side of the axial summit trough, and it would have sampled a number of geochemically distinct magma batches that were inefficiently mixed in the axial magma chamber. Although this type of single, geochemically heterogeneous eruption has been observed to occur in two successive eruptions at 17°30′S EPR [*Bergmanis et al*., 2007], this scenario seems less likely at 9°50′N EPR because this level of geochemical heterogeneity has not been observed in either the 1991–1992 or 2005–2006 eruptions. In addition, the 2005–2006 eruption, which covered the ridge crest up to 2 km from the axial summit trough in places (though in no places did it cover both sides of the axial summit trough to this distance),

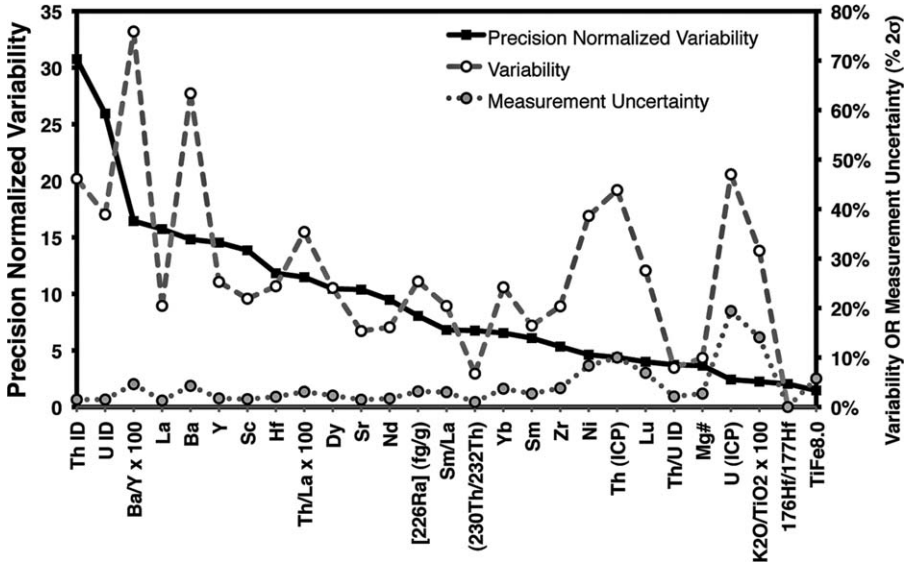

Figure 7. Precision-normalized natural variability (P_i/S_i) of select geochemical metrics (i) for dive 3974 lavas, ordered from highest to lowest, where P is the natural variability and S is the measurement uncertainty (also shown). Thorium and U abundances as determined by ID have the highest precision-normalized variability by a factor of ~1.5 and thus constitute the best available geochemical metrics for discriminating among individual eruptive units. It should be noted that the coefficient of variability (%) for TiFe8.0 is not shown because it is undefined; TiFe8.0 is already standardized to a mean of zero.

terminated primarily in pillowed flow fronts at its most distal points and was composed of sheet flow interiors (associated with the high effusion rates necessary to produce such extensive flows) [*Fundis et al.*, 2010]; whereas, the samples collected here were collected from sequences of pillowed flow fronts with lobate or sheet flow interiors.

[31] We also note that across the widest part of the 2005–2006 flow near 9°50.5′N ("central region") (Figure 1), which spans from ~1 km west to ~2.5 km east of the axial summit trough, molar Mg# and incompatible element ratios vary little [*Goss et al.*, 2010]. Samples from the western extent of the flow have Mg# as high as 60.1, decrease to as low as Mg#~58.3 near the center, and finally increase to Mg# ~60.2 near the eastern edge (mean Mg#~59.4 ± 1.1 (2σ), n=24); Ba/Y × 100 ranges from 28.1 to 24.8 to 27.7 (mean Ba/Y × 100~26.9 ± 2.1 (2σ), n=25) [*Goss et al.*, 2010]. Measured 2005–2006 samples from this flow lobe also have homogeneous $^{87}Sr/^{86}Sr$ (0.702465–0.702501), ε_{Nd} (10.5–10.6), and $^{208}Pb/^{206}Pb$ (2.063–2.064) isotope compositions that are indistinguishable from each other and similar to 1991–1992 lavas [*Goss et al.*, 2010]. The overall lack of compositional variability in the 2005–2006 central region contrasts from what is observed here in

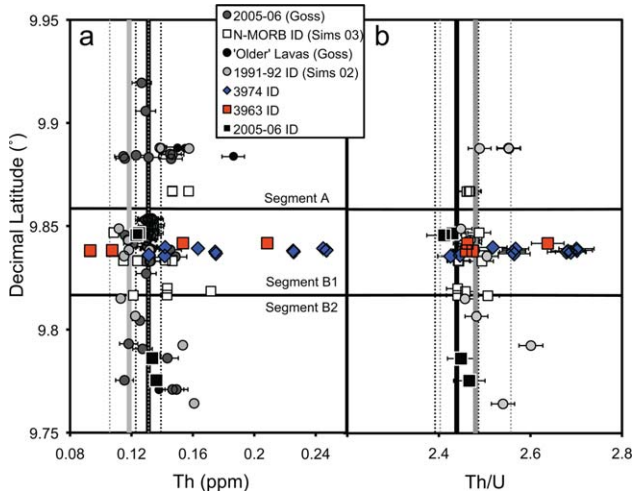

Figure 8. (a) Th (ppm) and (b) Th/U variations of dive 3974 and 3963 samples with latitude. Samples from the 1991–1992 [*Sims et al.*, 2002] and 2005–2006 [*Goss et al.*, 2010; this study] eruptions are shown for comparison, as are neo-volcanic zone samples in the region [*Goss et al.*, 2010; *Sims et al.*, 2003; *Waters et al.*, 2011]. Boundaries for fourth-order segments A, B1, and B2 as defined in *Haymon et al.* [1993] are shown. Vertical solid and dashed lines delimit the population means and standard deviations (2σ), respectively, within Segment B1 for the 1991–1992 and 2005–2006 eruptions. Because propagated uncertainties for Th/U measured by ICP-MS without ID are large (>10%), we only show Th/U as measured by ID.

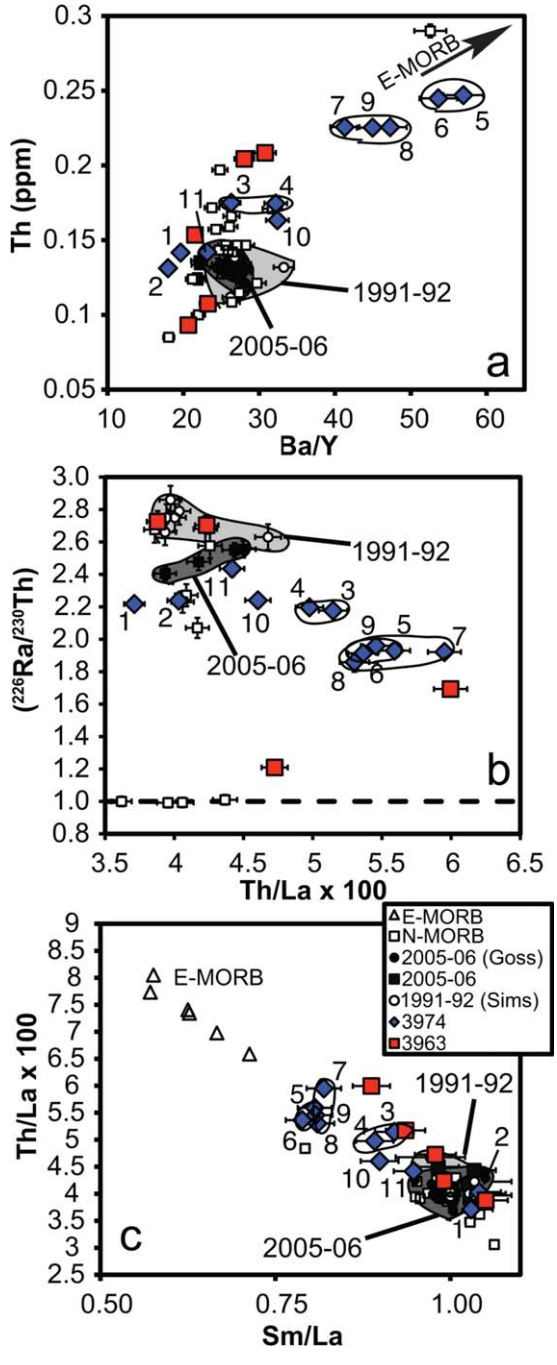

Figure 9. Variations in (a) Ba/Y × 100 versus Th (ppm), (b) Th/La × 100 versus (^{226}Ra/^{230}Th), and (c) Sm/La versus Th/La × 100 for dive 3974 and 3963 samples, 1991–1992 and 2005–2006 eruption samples collected within Segment B1 (shaded fields) [*Goss et al*., 2010; *Sims et al*., 2002], N-MORB samples collected outside of the axial summit trough from the 9°48′–9°54′N region [*Sims et al*., 2003; *Waters et al*., 2011], and E-MORB collected several kilometers east of the axial summit trough from 9°30′N to 9°35′N (Figure 9a and Figure 9c only; *Waters et al*. [2011]). Dive 3974 samples are numbered. Groups of dive 3974 samples that have indistinguishable Th abundances are circled. See text for details.

dive 3974 and 3963 samples and has been previously observed in this region, that lavas trend to progressively more evolved compositions further from the axial summit trough [e.g., *Kurras et al*., 2000]. One explanation for this observation is that eruptions as large as the 2005–2006 eruption are anomalous and not well represented in the neo-volcanic zone. The composition of the 2005–2006 eruption is interpreted as resulting from additional mixing and differentiation of residual liquids from the 1991–1992 eruption, largely based on the slightly more evolved compositions of 2005–2006 lavas compared to 1991–1992 lavas [*Goss et al*., 2010]. The evolution of lavas toward more primitive compositions from the edge of the neo-volcanic zone towards the axial summit trough may reflect increasing magma supply and decreasing differentiation during the recent past, or variations in the depth of melt initiation and mantle source Mg-Fe composition [*Sims et al*., 2002]. If the process responsible is increasing magma supply and decreasing differentiation, this would require decoupling of major elements from incompatible elements and isotopic variations that are primarily controlled by variations in melting and mantle mixing processes (see section 5.5).

[32] For all dive 3974 and 3963 lavas to have been produced during a single eruption, the magmatic system at 9°50′N would have had to be dramatically different at some time within the past 2 ka. Thus, either this putative single eruption scenario resulted from a series of pulses of geochemically distinct magma batches that repeatedly stalled at pillow fronts with the first pulse reaching farthest from the axis and each subsequent pulse stalling progressively closer to the axis (otherwise subsequent pulses would be paved over), or, more likely, these samples represent multiple eruptions.

[33] (2) *Ten geochemically distinct eruptions*. The alternative end member scenario is that each eruption sampled one geochemically distinct batch of magma (in particular with respect to Th and U abundances), thus requiring ten distinct eruptions to explain the 10 sampled flows. This is possible given the wide range and distinct geochemical compositions of individual flow shingles, which exceed that observed in both the 1991–1992 and 2005–2006 eruptions. However, both the 1991–1992 and 2005–2006 eruptions exhibit some geochemical variability (Figures 4, 5, 6, 8, and 9), and it is therefore possible that some of these samples erupted at the same time and represent fewer than ten eruptions. Greater documentation of the

geochemical variability within individual eruptions is required to rule out this scenario.

[34] (3) *Six eruptions*. The scenario that we favor is one involving six distinct eruptions, some of which sample multiple batches of magma that are analytically distinguishable with respect to Th and U abundances, but not so different that they could not be related to each other by subtle variations in mixing or differentiation. In particular, samples 3974-1 and 2 may have originated from the same eruption, particularly given their close proximity and similar geochemistry. We also think it is plausible that samples 3974-5 and 6 and 3974-7, 8, and 9 originated from different pulses of the same eruption, as they are similarly enriched and located in adjacent, though physically distinct, flow bodies. Samples 3974-10 and 11 also have reasonably similar compositions and are close enough together that they could be explained by a single flow. Samples 3974-1 and 2 and 3974-10 and 11 could be from the same eruption, yet it seems less likely given their geographic disparity, though we cannot rule out tube flow to 2 km off-axis [e.g., *Applegate and Embley*, 1992].

[35] On the east side of the axis, sample 3963-5 is distinct from 3963-9 and 10 but may be related to the trend of enrichment observed on the west side (3974-5 through 3974-9). If these samples were collected from the products of a single eruption, the greater compositional variability could be due to an episode of decreased magma supply, increased magma chamber crystallinity, and thus decreased connectivity and inhibited mixing. Alternatively, it is possible that the small differences in enrichment observable between samples 3974-5 and 6, 3974-7, 8, and 9, and 3963-5 are due to small inter-eruption differences in crustal mixing and differentiation of related liquids, as observed between the 1991–1992 and 2005–2006 eruptions [*Goss et al*., 2010]. Given their location and geochemical similarity to the 1991–1992 and 2005–2006 eruptions, we believe that samples 3963-9 and 10 are probably associated with the latest series of eruptions. Sample 3963-6 is also distinctly older based on both U-series and paleomagnetic intensity measurements [*Bowles et al*., 2006].

4.3. The Origin of Shingled Terrain

[36] Side-scan sonar, magnetic, and U-series and magnetic paleointensity dating studies at 9°50′N EPR have shown that the neo-volcanic zone extends up to ~2–4 km on either side of the axial summit trough [*Bowles et al*., 2006; *Escartin et al*., 2007; *Fornari et al*., 1998; *Goldstein et al*., 1994; *Schouten et al*., 1999; *Sims et al*., 2003; *Soule et al*., 2009]. However, the formation of the shingled terrain within the neo-volcanic zone has not been satisfactorily explained. The thickening of seismic layer 2A, interpreted to be the extrusive crust, within the neo-volcanic zone [e.g., *Harding et al*., 1993] can be well explained by a bimodal lava emplacement model in which roughly half of the extrusive volume is made up of small lava flows confined to the axial summit trough and half is made up of large flows that spill onto the ridge flanks [*Hooft et al*., 1996]. Presumably, shingle-textured terrain arises from some combination of stratigraphic superposition of flows, stagnation of individual flows forming pillow fronts and subsequent breakouts, and direct off-axis emplacement by lava transport through existing tubes, but the relative contributions of these different mechanisms remains unclear.

[37] There is sufficient evidence from side-scan sonar and seafloor observations to rule out an off-axis eruptive origin for all samples except 3974-1, which is geochemically similar to sample 2771-1 from *Sims et al*. [2003], and both samples may be related to a nearby off-axis pillow mound (Figures 2a and 2b). Although there is some evidence for breakouts from pillow lava fronts (e.g., sample 3974-7), these breakouts do not appear to be a ubiquitous feature at flow fronts, and in general, do not produce extensive lava units. This is consistent with recent mapping of the 2005–2006 eruption that documented pillow lavas primarily at flow termini [*Fundis et al*., 2010]. Because dive 3974 and 3963 lava ages are young enough that we cannot statistically resolve sample ages within a ~2 kyr age population, we cannot discern whether the flows sampled result primarily from simple superposition of surface flows or from transport through lava tubes, which have been observed in the walls of the axial summit trough [*Gregg and Fornari*, 1998; *Haymon et al*., 1993]. Both surface and tube transport of flows could cause younger flows to be emplaced farther from the axis than older flows. For example, axis-parallel or oblique surface flow of lava due to variable seafloor topography or from fault/pillow ridge embankment can result in lavas of younger age being emplaced further off-axis than older flows [cf., *Escartin et al*. 2007, Figure 3d]. Thus, even if higher precision lava ages *could* be determined for such young lavas, this type of plan-view lava age distribution is not diagnostic of subsurface lava transport and does not necessarily preclude simple superposition of surface flows.

4.4. The Youth of the Neo-Volcanic Zone

[38] The age constraints from this study and other dating studies at 9°50′N EPR [*Bowles et al*., 2006; *Sims et al*., 2003] are consistent with the region up to ~2 km (~36 ka nominal spreading age) on either side of the axial summit trough at 9°50′N EPR being mostly covered by lavas less than ~2 ka. Only one lava sample (3963-6) that we dated appears to be older than ~2 ka, but with an estimated ^{230}Th-^{226}Ra model age of ~5 ka, it is still much younger than its nominal spreading age (~31 ka). Given similar age constraints obtained from ^{238}U-^{230}Th and ^{230}Th-^{226}Ra model age dating in other studies [*Sims et al*., 2003; *Waters et al*., 2011], it appears that lavas outside the neovolcanic zone are older (>5–10 ka) than lavas within the neo-volcanic zone. In addition, they typically have equilibrium (^{226}Ra/^{230}Th) values and magnetic paleointensities that are lower than the present-day field, and they have ^{238}U-^{230}Th or ^{235}U-^{231}Pa model ages that cannot be resolved from the spreading rate "age" (note this is exclusive of two samples with small ^{226}Ra excesses collected 10s of kilometers from the axial summit trough at 9°19′N and 9°30′N EPR; *Turner et al*. [2011]). At 9°50′N, there is a general sense of an abrupt increase in lava ages from <2 ka within the neovolcanic zone to >8 ka outside of the neovolcanic zone.

[39] This abrupt change in lava ages might suggest that the 9°50′N EPR region has experienced a period of increased volcanic activity for the past ~2 ka, with relatively frequent flows reaching ~1–2 km on either side of the axial summit trough. This model is consistent with recent observations of the 2005–2006 flow distribution and axial summit trough geometry at 9°N to 10°N EPR [*Soule et al*., 2009] and evidence from 17° to 18°S EPR [*Cormier et al*., 2003] that support cyclic changes in magmatism over time. However, *Bowles et al*. [2006] found that age offsets of ~5–10 ka between neo-volcanic lavas and lavas on highly tectonized "old" crust can be well explained by a lava emplacement model that links eruption volume linearly with time between eruptions. In this model, the time between eruptions is not linked to the spreading rate but is instead determined by a standard gamma distribution in flow length with a median scaled to the median time between eruptions. Thus, longer flows occur after longer repose times between eruptions. *Bowles et al*. [2006] found that a ~70 year median eruption recurrence interval provides a good match to their magnetic paleointensity observations. Their model shows that the time elapsed between flows preserved on the seafloor beyond ~1 km from the axial summit trough is >250 years (see Figure 13e from *Bowles et al*. [2006]). Although uncertain because of the lack of precise ages, the number of flows we think we observe reaching ~1–2 km from the axial summit trough in this location (~3–5 per <2 ka) is of the same order as that predicted by the model of *Bowles et al*. [2006] (2–3 per 2 ka). Thus, we favor this model, which, notably, does *not* require increased volcanic activity over the past ~2 ka. However, this requires that the flows that dives 3974 and 3963 traversed provide a representative picture of time-integrated volcanism occurring near 9°50′N EPR, as only a single large event of low probability is required to apparently bias the effects of a stochastic process (e.g., the 2005–2006 eruption flowed to 3 km in one location). Thus, more spatially comprehensive geological and geochemical surveys utilizing and integrating ^{230}Th-^{226}Ra methods with higher resolution age dating methods (e.g., ^{226}Ra-^{210}Pb and magnetic paleointensities), and/or refinement of the ^{230}Th-^{226}Ra model age dating method with better constraints on zero-age, initial disequilibria, may be required to verify this interpretation.

4.5. Origin of Variations in Melt Compositions

[40] One of the most interesting features of the present data set is that incompatible element abundances and ratios, Sr, Nd, and Hf isotope compositions, and U-series disequilibria appear to be correlated in a suite of N-MORB erupted within the last ~2 ka. As a whole, these compositions appear to trend towards the more enriched compositions observed in E-MORB collected from outside of the neo-volcanic zone at 9°N to 10°N EPR and near the axial summit trough at the small overlapping spreading center at 9°37′N [*Perfit and Chadwick*, 1998; *Perfit et al*., 1994; *Smith et al*., 2001; *Volpe and Goldstein*, 1993; *Waters et al*., 2011]. The compositional variability observed among dive 3974 and 3963 lavas over this time frame (Figures 4–6, 8, and 9) suggests relatively rapid changes in the magma compositions supplied to and stored in the axial magma chamber. This interpretation is similar to the observations of rapid changes in geochemical variability at 17°30′S EPR [*Bergmanis et al*., 2007], although we cannot resolve if geochemical variability due to magmatic processes is occurring on time scales more rapid than the eruption rate.

[41] We observe variability in incompatible element abundances across fourth-order segment boundaries in the 9°50′N EPR region, and this

probably partly reflects along-axis axial magma chamber segmentation, as incompatible element abundances within segment B1 are nearly constant for both 1991–1992 and 2005–2006 eruptions (Figure 8a). Thus, the variation in Th and U abundances in dive 3974 and 3963 lavas could potentially be due to changing crustal magmatic conditions over time within 4th order Segment B1 (Figure 8a). However, in contrast to incompatible element abundances, long-lived radiogenic isotope ratios do not reflect crustal differentiation processes and are indicative of mantle source composition and mixing processes only. Ratios of highly incompatible elements (e.g., Th/U) are similarly insensitive to fractional crystallization [i.e., $(Th/U_{melt})/(Th/U_{initial}) = F^{DTh-DU}$, so since D_{Th}-D_U is small, Th/U fractionation in the melt will be small] and this is demonstrated well by the broad negative correlation between Th/U and ε_{Nd} (Figure 5b). Within segment B1, dive 3974 and 3963 sample Th/U and ε_{Nd} vary and extend to more enriched compositions than samples associated with the 1991–1992 and 2005–2006 flows, demonstrating that a significant component of the incompatible element variability observed here over even these short time scales (100s to 1000s of years) ultimately reflects the presence of a geochemically heterogeneous mantle source (Figure 8b), which has been observed in other locations along the EPR [e.g., *Castillo et al*., 2000; *Fornari et al*., 1988; *Macdougall and Lugmair*, 1986; *Prinzhofer et al*., 1989; *Zindler et al*., 1984].

[42] *Sims et al*. [2002] explained U-series variations among young axial N-MORB from 9 to 10°N EPR, namely the negative correlation between (^{230}Th/^{238}U) and (^{226}Ra/^{230}Th), by mixing of deep, low-degree melts and shallow, high-degree melts of a homogeneous mantle source, as all samples considered had indistinguishable ^{87}Sr/^{86}Sr, ^{143}Nd/^{144}Nd, ^{176}Hf/^{177}Hf, and ^{208}Pb/^{206}Pb. Deep, low-degree melts of a garnet-bearing source with large ^{230}Th excesses and small ^{226}Ra excesses were interpreted to be channelized and transported rapidly towards the crust (similar to dynamic melting) and mixed with shallowly equilibrated high-degree melts with small ^{230}Th excesses and large ^{226}Ra excesses (essentially produced by chromatographic melting). Unlike *Sims et al*. [2002], we observe small, correlated variations among long-lived radiogenic isotopes that are also correlated with incompatible element and U-series variations. Thus, our data are consistent with their model, with the addition that the deep melts sample an isotopically enriched mantle source (i.e., lower ^{226}Ra excesses, higher ^{230}Th excesses, higher incompatible element abundances and ratios, and enriched Sr, Nd, Hf isotope compositions relative to more shallowly equilibrated melts). Indeed, recent melt modeling studies of lavas from nearby 9°30′ to 9°35′N EPR [*Waters et al*., 2011], seamount 6 at 12°45′N EPR [*Brandl et al*., 2012], Iceland [*Koorneef et al*., 2012; *Stracke and Bourdon*, 2009], and from the fossil Phoenix Ridge and Galapagos Rise [*Haase et al*., 2011a, 2011b], have shown that mixing of melts derived from a heterogeneous mantle source in which more fusible, enriched mantle lithologies (e.g., pyroxenite/eclogite) melt preferentially and are better represented in lower degree melts can explain observed incompatible element and long-lived radiogenic isotope variations in MORB. At 9°50′N EPR, where the magma supply is thought to be robust relative to the rest of the 9°N to 10°N EPR segment, we further elaborate that the geochemical variability of lavas probably results from more subtle fluctuations in the relative mixing contributions of enriched and depleted melts derived from a heterogeneous mantle source. Greater geochemical variability in the 9°N to 10°N region, such as the variation from N-MORB to E-MORB observed in older lavas collected several kilometers east of the axial summit trough at 9°30′N–9°35′N EPR, may occur over longer time scales (ka to 10s of ka) [cf., *Waters et al*., 2011] than that represented by lavas within the present-day neo-volcanic zone at 9°50′N. These longer-term variations probably reflect larger variations in magma supply and less efficient mixing of depleted and enriched melts in crustal magma bodies in the past.

5. Conclusions

[43] To determine how "shingled," neo-volcanic terrain at 9°N to 10°N EPR is formed, we measured major and trace elements and ^{87}Sr/^{86}Sr, ^{143}Nd/^{144}Nd, ^{176}Hf/^{177}Hf, and ^{238}U-^{230}Th-^{226}Ra isotope compositions for samples collected during two dive traverses across the ridge crest at 9°50′N EPR. From our observations, we make the following conclusions:

(1) Scatter about the zero-age trend line defining initial U-series disequilibria prohibits resolution of model ages <2 ka, and only one sample (3963-6) has a model age that is statistically distinct from the zero-age trend line at the 95% confidence limit. All other samples are indistinguishable from the zero-age population, indicating that the neo-volcanic zone at 9°50′N EPR,

as defined by side-scan sonar imaging and the central magnetic anomaly high, is <2 ka.

(2) Because the extent of intra- and inter-eruption geochemical variability is insufficiently known at this time, we cannot unambiguously identify discrete eruptive units on the basis of geochemistry alone. However, based on the currently available geochemical data for the 1991–1992 and 2005–2006 eruptions along with inferences from geological observations, we posit that dive 3974 and 3963 lavas may represent between 6 and 10 eruptions.

(3) Dive 3963 and 3974 lavas exhibit a greater range in incompatible element abundances and Sr, Nd, Hf, and U-series isotopic variability than has previously been observed in individual eruptions of N-MORB at 9°N to 10°N, and variations among incompatible elements and ratios and Sr, Nd, Hf, and U-series isotopic compositions are correlated and trend to E-MORB type compositions. We interpret these variations in chemistry as reflecting short-term variability in a coupled progressive melting-mixing process that samples a heterogeneous mantle source.

(4) The high precision-normalized variability of Th and U ID abundances suggests that they are a powerful complement to mapping of seafloor eruptive units. However, proper interpretation of Th and U ID "mapping" requires comparison with temporally sensitive (<10s to 1000s of years) age proxies utilizing (^{226}Ra/^{230}Th), (^{210}Pb/^{226}Ra), and magnetic paleointensities.

(5) Although current methods for dating MORB all suffer shortcomings, combining these methods can help to limit possible sample ages, and improving our understanding of how petrogenetic processes establish initial ^{238}U–^{230}Th-^{226}Ra disequilibria at the time of eruption will help to better refine model age techniques. At present, ^{230}Th-^{226}Ra disequilibria may be more useful for resolving lava ages where eruptions are less frequent, such as at slow or ultra-slow spreading ridges [cf., *Standish and Sims*, 2010].

Acknowledgments

[44] This study was funded by NSF OCE-0623838 to K.W.W. Sims and S.A. Soule and NSF OCE-0527053 to K.W.W. Sims. J. Blichert-Toft acknowledges financial support from the French Agence Nationale de la Recherche (grant M&Ms – Mantle Melting – Measurements, Models, Mechanisms). CLW thanks Jeremy Inglis and Ethan Baxter for assistance with TIMS Sr isotopic analyses at Boston University, Jurek Blusztajn for assistance with Sr isotopic analyses at WHOI, and Erin Philips-Writer for assistance with U and Th analyses at the University of Wyoming. Chris Boynton and Louise Bolge are gratefully acknowledged for analytical assistance with the LA-ICP-MS analyses at LDEO. Paul Henderson, Matt Charette, and Christian Miller are especially thanked for their help preparing a new ^{228}Ra spike for isotope dilution measurements at WHOI. Tim Elliot and Chris Coath are thanked for the smooth running of the BIG labs. Mike Perfit is thanked for providing dive 3974 and 3963 samples. This study benefited from constructive reviews by J. Koorneef, K. Rubin, and P. Brandl.

References

Applegate, B., and R. W. Embley (1992), Submarine tumuli and inflated tube-fed flows on Axial Volcano, Juan de Fuca Ridge, *Bull. Volcanol.*, *54*, 447–458.

Ball, L., K. Sims, S. Weyer, and J. Schweiters (2008), Measurement of 234U/238U and 230Th/232Th in volcanic rocks using the Neptune PIMMS, *J. Anal. At. Spectrom.*, *23*, 173–180, doi:10.1039/b703193a.

Ballard, R. D., R. T. Holcomb, and T. H. van Andel (1979), The Galapagos Rift at 86°W: 3. Sheet flows, collapse pits, and lava lakes of the rift, *J. Geophys. Res.*, *84*(B10), 5407–5422.

Beattie, P. (1993), Uranium-thorium disequilibria and partitioning on melting of garnet peridotite, *Earth Planet. Sci. Lett.*, *363*, 63–65.

Bergmanis, E. C., J. Sinton, and K. H. Rubin (2007), Recent eruptive history and magma reservoir dynamics on the southern East Pacific Rise at 17°30'S, *Geochem. Geophys. Geosyst.*, *8*, Q12O06, doi:10.1029/2007GC001742.

Blichert-Toft, J. (2001), On the Lu-Hf isotope geochemistry of silicate rocks, *Geostandards Newsletter*, *25*, 41–56.

Blichert-Toft, J., and F. Albarède (1997), The Lu-Hf isotope geochemistry of chondrites and the evolution of the mantle-crust system, *Earth Planet. Sci. Lett.*, *148*, 243–258.

Blichert-Toft, J., and Albarède, F. (2009), Mixing of isotopic heterogeneities in the Mauna Kea plume conduit, *Earth Planet. Sci. Lett.*, *282*, 190–200.

Blichert-Toft, J., C. Chauvel, and F. Albarède, (1997), Separation of Hf and Lu for high-precision isotope analysis of rock samples by magnetic sector-multiple collector ICP-MS, Contrib. *Mineral. Petrol.*, *127*, 248–260.

Blichert-Toft, J., A. Agranier, M. Andres, R. Kingsley, J.-G. Schilling, and F. Albarède (2005), Geochemical segmentation of the Mid-Atlantic Ridge north of Iceland and ridge-hot spot interaction in the North Atlantic, *Geochem. Geophys. Geosyst.*, *6*, Q01E19, doi:10.1029/2004GC000788.

Blundy, J., and B. Wood (2003), Mineral-melt partitioning of uranium, thorium and their daughters, *Rev. Mineral. Geochem. 52*, 59–123.

Bowles, J., J. G. Gee, D. V. Kent, M. R. Perfit, S. A. Soule, and D. J. Fornari (2006), Paleointensity applications to timing and extent of eruptive activity, 9°–10°N East Pacific Rise, *Geochem. Geophys. Geosyst.*, *7*, Q06006, doi:10.1029/2005GC001141.

Brandl, P. A., C. Beier, M. Regelous, W. Abouchami, K.M. Haase, D. Garbe-Shonberg, and S.J.G. Galer (2012), Volcanism on the flanks of the East Pacific Rise: Quantitative constraints on mantle heterogeneity and melting processes, *Chem. Geol.*, *298-299*, 41–56.

Cann, J. R., and D. K. Smith (2005), Evolution of volcanism and faulting in a segment of the Mid-Atlantic Ridge at 25°N, *Geochem. Geophys. Geosyst.*, *6*, Q09008, doi:10.1029/2005GC000954.

Carlut, J., M.-H. Cormier, D. V. Kent, K. E. Donnelly, and C. H. Langmuir (2004), Timing of volcanism along the northern East Pacific Ries based on paleointensity experiments on basaltic glasses, *J. Geophys. Res.*, *109*, B04104, doi:10.1029/2003/JB002672.

Castillo, P. R., E. Klein, J. Bender, C. Langmuir, S. Shirey, R. Batiza, and W. White (2000), Petrology and Sr, Nd, and Pb isotope geochemistry of mid-ocean ridge basalt glasses from the 11°45'N to 15°00'N segment of the East Pacific Rise, *Geochem. Geophys. Geosyst.*, *1*(11), 1011, doi:10.1029/1999GC000024.

Chauvel, C., and J. Blichert-Toft (2001), A hafnium isotope and trace element perspective on melting of the depleted mantle, *Earth Planet. Sci. Lett.*, *190*, 137–151.

Christeson, G. L., G. M. Purdy, and G. J. Fryer (1994), Seismic constraints on shallow crustal emplacement processes at the fast-spreading East Pacific Rise, *J. Geophys Res.*, *99*, 17,957–17,973.

Christeson, G. L., G. M. Kent, G. M. Purdy, and R. S. Detrick (1996), Extrusive thickness variability at the East Pacific Rise, 9°-10°N, constraints from seismic techniques, *J. Geophys. Res.*, *101*, 2859–2873.

Cochran, J. R., D. J. Fornari, B. J. Coakley, R. Herr, and M. A. Tivey (1999), Continuous near-bottom gravity measurements made with a BGM-3 gravimeter in DSV Alvin on the East Pacific Rise crest near 9°30'N and 9°50'N, *J. Geophys. Res.*, *104*, 10,841–10,861.

Cooper, K. M., S. J. Goldstein, K. W. W. Sims, and M. T. Murrell (2003), Uranium-series chronology of Gorda Ridge volcanism: new evidence from the 1996 eruption, *Earth Planet. Sci. Lett.*, *206*, 459–475.

Cooper, L. B., T. Plank, R. J. Arculus, E. H. Hauri, P. S. Hall, and S. W. Parman (2010), High-Ca boninites from the active Tonga Arc, *J. Geophys. Res.*, *115*, B10206, doi:10.1029/2009JB006367.

Cormier, M.-H., W. B. F. Ryan, A. K. Shah, W. Jin, A. M. Bradley, and D. R. Yoerger (2003), Waxing and waning volcanism along the East Pacific Rise on a millennium time scale, *Geology*, *31*(7), 633–636.

Elkins, L. E., G. A. Gaetani, and K. W. W. Sims (2008), Partitioning of U and Th during garnet pyroxenite partial melting: Constraints on the source of alkaline ocean island basalts, *Earth Planet. Sci. Lett. 265*, 270–286.

Elkins, L. J., et al. (2011), Understanding melt generation beneath the slow-spreading Kolbeinsey Ridge using 238U, 230Th, and 231Pa excesses, *Geochim. Cosmochim. Acta*, *75*, 6300–6329.

Elliot, T. (1997), Fractionation of U and Th during mantle melting: a reprise, *Chem. Geol. 139*, 165–183.

Escartin, J., S. A. Soule, D. J. Fornari, M. A. Tivey, and H. Schouten (2007), Interplay between faults and lava flows in construction of the upper oceanic crust: The East Pacific Rise crest 9°25'-9°58'N, *Geochem. Geophys. Geosyst.*, *8*, Q06005, doi: 10.1029/2006GC001399.

Fornari, D. J., et al. (1988), Geochemical and structural studies of the Lamont seamounts: seamounts as indicators of mantle processes, *Earth Planet. Sci. Lett.*, *89*, 63–83.

Fornari, D. L., R. Haymon, M. Perfit, T. K. P. Gregg, and M. H. Edwards (1998), Axial summit trough of the East Pacific Rise, 9–10°N: Geological characteristics and evolution of the axial zone on fast spreading mid-ocean ridges, *J. Geophys. Res.*, *103*, 9827–9855.

Fornari, D. L., et al. (2004), Submarine Lava Flow Emplacement at the East Pacific Rise 9°50'N: Implications for uppermost ocean crust stratigraphy and hydrothermal fluid circulation, in *Mid-Ocean Ridges: Hydrothermal Interactions between the Lithosphere and Oceans*, *Geophys. Monogr. Ser*., vol. 148, edited by C. R. German, J. Lin, and L. M. Person, pp. 311, AGU, Washington, D. C.

Fundis, A. T., S. Soule, D. J. Fornari, and M. R. Perfit (2010), Paving the seafloor: Volcanic emplacement processes during the 2005–2006 eruptions at the fast spreading East Pacific Rise, 9°50'N, *Geochem. Geophys. Geosyst.*, *11*, Q08024, doi: 10.1029/2010GC003058.

Goldstein, S. J., M. T. Murrell, D. R. Janecky, J. R. Delaney, and D. Clague (1992), Geochronology and petrogenesis of MORB from the Juan de Fuca and Gorda Ridges by 238U-230Th disequilibrium, *Earth Planet. Sci. Lett.*, *109*, 255–272.

Goldstein, S. J., M. T. Murrell, and R. W. Williams (1993), ^{231}Pa and ^{230}Th chronology of Mid-Ocean Ridge Basalts, *Earth Planet. Sci. Lett.*, *115*, 151–160.

Goldstein, S. J., M. R. Perfit, R. Batiza, D. J. Fornari, and M. T. Murrell, (1994), Off-axis volcanism at the East Pacific Rise detected by uranium-series dating of basalts, *Nature*, *367*, 157–159.

Goss, A. R., M. R. Perfit, W. I. Ridley, K. H. Rubin, G. D. Kamenov, S. A. Soule, and A. Fundis (2010), Geochemistry of lavas from the 2005–2006 eruption at the East Pacific Rise, 9°46'N–9°56'N: Implications for ridge crest plumbing and decadal changes in magma chamber compositions, *Geochem. Geophys. Geosyst.*, *11*, Q05T09, doi: 10.1029/2009GC002977.

Gregg, T. K. P., and J. H. Fink (1995), Quantification of submarine lava-flow morphology through analog experiments, *Geology*, *23*(1), 73–76.

Gregg, T. K .P., and J. H. Fink (2000), A laboratory investigation into the effects of slope on lava flow morphology, *J. Volcanol. Geotherm. Res.*, *96*, 145–159.

Gregg, T. K. P., and D. J. Fornari (1998), Long submarine lava flows: Observations and results from numerical modeling, *J. Geophys. Res.*, *103*(B11), 27,517–27,531.

Gregg, T. K. P., D. J. Fornari, M. R. Perfit, R. M. Haymon, and J. H. Fink (1996), Rapid emplacement of a mid-ocean ridge lava flow on the East Pacific Rise at 9°46'-51'N, *Earth Planet. Sci. Lett.*, *144*, E1–E7.

Haase, K. M., C. Beier, S. Fretzdorff, P. T. Leat, R. A. Livermore, T. L. Barry, J. A. Pearce, and F. Hauff (2011a), Magmatic evolution of a dying spreading axis: evidence for the interaction of tectonics and mantle heterogeneity from the fossil Phoenix Ridge, Drake Passage, *Chem. Geol.*, *280*(1-2), 115–125.

Haase, K. M., M. Regelous, R. A. Duncan, P. A. Brandl, N. Stroncik, and I. Grevemeyer (2011b), Insights into mantle composition and mantle melting beneath mid-ocean ridges from postspreading volcanism on the fossil Galapagos Rise, *Geochem. Geophys. Geosyst.*, *12*, Q0AC11, doi:10.1029/2010GC003482.

Harding, A. J., G. M. Kent, and J. A. Orcutt (1993), A multichannel seismic investigation of upper crustal structure at 9°N on the East Pacific Rise: Implications for crustal accretion, *J. Geophys. Res.*, *98*, 13,925–13,944.

Hauri, E. H., T. P. Wagner, and T. L. Grove (1994), Experimental and natural partitioning of Th, U, Pb, and other trace

elements between garnet, clinopyroxene, and basaltic melts, *Chem. Geol. 117*, 149–166.

Haymon, R. M., D. J. Fornari, M. H. Edwards, S. C. Carbotte, D. Wright, and K. C. Macdonald (1991), Hydrothermal vent distribution along the East Pacific Rise Crest (9°09'–54'N) and its relationship to magmatic and tectonic processes on fast-spreading mid-ocean ridges, *Earth Planet. Sci. Lett.*, *104*, 513–534.

Haymon, R. M., D. J. Fornari, K. L. Von Damm, M. D. Lilley, M. R. Perfit, and J. M. Edmond (1993), Volcanic eruption of the mid-ocean ridge along the East Pacific Rise crest at 9° 45-45'N: Direct submersible observations of seafloor phenomena associated with an eruption event in April, 1991, *Earth Planet. Sci. Lett. 119*, 85–101.

Henderson, G. M., A. S. Cohen, and R. K. Onions (1993), U-234/U-238 ratios and Th-230 ages for hateruma atoll corals—Implications for coral diagenesis and seawater U-234/U-238 ratios, *Earth Planet. Sci. Lett.*, *115*, 65–73.

Hoffmann, D., J. Prytulak, D. Richards, T. Elliot, C. D. Coath, P. L. Smart, and D. Scholz (2007), Procedures for accurate U and Th isotope measurements by high precision MC-ICPMS, *Int. J. Mass Spectrom. 264*, 97–109.

Hon, K., J. Kauahikaua, R. Denlinger, and K. McKay (1994), Emplacement and inflation of pahoehoe sheet flows: Observations and measurements of active lava flows on Kilauea Volcano, Hawaii, *Geol. Soc. Am. Bull.*, *106*, 351–370.

Hooft, E. E. E., H. Schouten, and R. S. Detrick (1996), Constraining crustal emplacement processes from the variation in seismic layer 2A thickness at the East Pacific Rise, *Earth Planet. Sci. Lett.*, *142*, 289–309.

Jarosewich, E., J. A. Nelen, and J. A. Norberg (1980), Reference samples for electron microprobe analysis, *Geostand. Newslett.*, *4*, 43–47.

Kelley, K. A., T. Plank, J. Ludden, and H. Staudigel (2003), Composition of altered oceanic crust at ODP Sites 801 and 1149, *Geochem. Geophys. Geosyst.*, *4*(6), 1–21, doi:10.1029/2002GC000435.

Koorneef, J. M., A. Stracke, B. Bourdon, M. A. Meier, K. P. Jochum, B. Stoll, and K. Gronvold (2012), Melting of a two-component source beneath Iceland, *J. Petrol.*, *53*(1), 127–157.

Ku, T.-L., K. G. Knauss, and G. G. Mathieu (1977), Uranium in open ocean: Concentration and isotopic composition, *Deep Sea Res.*, *24*, 1005–1017.

Kurras, G. J., D. J. Fornari, M. H. Edwards, M. J. Perfit, and M. C. Smith (2000), Volcanic morphology of the East Pacific Rise Crest 9°49–52': Implications for volcanic emplacement processes at fast-spreading mid-ocean ridges, *Mar. Geophys. Res.*, *21*, 23–41.

LaTourette, T. Z., A. K. Kennedy, and G. J. Wasserburg (1993), Uranium-thorium fractionation of garnet—evidence for a deep source and rapid rise of oceanic basalts, *Science*, *261*, 739–742.

Lundstrom, C. C. (2003), Uranium-series disequililbria in mid-ocean ridge basalts: Observations and models of basalt genesis, in *Uranium-Series Geochemistry*, edited by B. Bourdon, G. M. Henderson, C. C. Lundstrom, and S. P. Turner, vol. 52, pp. 175–214, The Mineral. Soc. of Am., Washington, D. C.

Lundstrom, C. C., D. E. Sampson, M. R. Perfit, J. Gill, and Q. Williams (1999), Insights into mid-ocean ridge basalt petrogenesis: U-series disequilibria from the Siqueiros Transform, Lamont Seamounts, and East Pacific Rise, *J. Geophys. Res.*, *104*, 13,035–13,048.

Macdougall, J. D., and G. W. Lugmair (1986), Sr and Nd isotopes in basalts from the East Pacific Rise: significance for mantle heterogeneity, *Earth Planet. Sci. Lett.*, *77*, 273–284.

Maclennan, J., D. McKenzie, F. Hilton, K. Gronvold, and N. Shimizu (2003), Geochemical variability in a single flow from northern Iceland, *J. Geophys. Res.*, *108*(B1), 21, doi:10.1029/2000JB000142.

McKenzie, D. (1985), 230Th-238U disequilibrium and the melting processes beneath ridge axes, *Earth Planet. Sci. Lett.*, *72*, 149–157.

Perfit, M. R., and W. W. Chadwick Jr. (1998), Magmatism at mid-ocean ridges: Constraints from volcanological and geochemical investigations, in *Faulting and Magmatism at Mid-Ocean Ridges*, edited by W. R. Buck, P. T. Delaney, J. A. Karson, and Y. Lagabrielle, Geophys. Monogr. Ser. 106, pp. 59–115, AGU, Washington, D. C.

Perfit, M., D. Fornari, M. Smith, J. Bender, C. Langmuir, and R. Haymon (1994), Small-scale spatial and temporal variations in MORB geochemistry and implications for ridge crest magmatic processes, *Geology*, *22*, 375–379.

Pertermann, M., M. M. Hirschmann, L. Hametner, K. Gunther, and M. W. Schmidt (2004), Experimental determination of trace element partitioning between garnet and silica-rich liquid during anhydrous partial melting of MORB-like eclogite, *Geochem. Geophys. Geosyst. 5*, Q05A01, doi:10.1029/2003GC000638.

Prinzhofer, A., E. Lewin, and C. J. Allegre (1989), Stochastic melting of the marble cake mantle: evidence from local study of the East Pacific Rise at 12°50'N, *Earth Planet. Sci. Lett.*, *92*, 189–206.

Reynolds, J. R., C. H. Langmuir, J. F. Bender, J. A. Kastens, and W. B. F. Ryan (1992), Spatial and temporal variability in the geochemistry of basalts from the East Pacific Rise, *Nature*, *359*, 493–499.

Rhodes, M. (1983), Homogeneity of lava flows: Chemical data for historic Mauna Loan eruptions, *J. Geophys. Res.*, *88*, A869–A879.

Rhzanov, Y., L. Mayer, S. Beaulieu, T. Shank, S. A. Soule, and D. J. Fornari (2006), Deep-sea geo-referenced video mosaics, paper presented at OCEANS 2006, doi:10.1109/OCEANS.2006.307018.

Richter, S. and S. A. Goldberg (2003), Improved techniques for high accuracy isotope ratio measurements of nuclear materials using thermal ionization mass spectrometry, *Int. J. Mass Spectrom.*, *229*, 181–197.

Robinson, L. F., N. S. Belshaw, and G. M. Henderson (2004), U and Th concentrations and isotope ratios in modern carbonates and waters from the Bahamas, *Geochim. Cosmochim. Acta*, *68*(8), 1777–1789.

Rubin, K. H., and J. D. MacDougall (1990), Dating of neovolcanic MORB using (226Ra/230Th) disequilibrium, *Earth Planet. Sci. Lett.*, *101*, 313–321.

Rubin, K. H., J. D. MacDougall, and M. R. Perfit (1994), 210Po-210Pb dating of recent volcanic eruptions on the sea floor, *Nature*, *368*, 841–844.

Rubin, K. H., M. C. Smith, E. C. Bergmanis, M. R. Perfit, J. M. Sinton, and R. Batiza (2001), Geochemical heterogeneity within mid-ocean ridge lava flows: insights into eruption, emplacement and global variations in magma generation, *Earth Planet. Sci. Lett.*, *188*, 349–367.

Rubin, K. H., I. van der Zander, M. C. Smith, and E. C. Bergmanis (2005), Minimum speed limit for ocean ridge magmatism from 210Pb-226Ra-230Th disequilibria, *Nature*, *437*, 534–538.

Rubin, K. H., M. Tolstoy, D. J. Fornari, R. P. Dziak, S. A. Soule, F. Waldhauser, K. L. Von Damm (2008), Integrating radiometric, geophysical and thermal signals of volcanic unrest and eruption in 2005–06 at 9 deg 50'N EPR, Eos Trans. AGU, 89, Fall Meet. Suppl., Abstract # B23F-07.

Salters, V. J. M., and J. E. Longhi (1999), Trace element partitioning during the initial stages of melting beneath mid-ocean ridges, *Earth Planet. Sci. Lett. 166*, 15–30.

Salters, V. J. M., J. E. Longhi, and M. Bizimis (2002), Near mantle solidus trace element partitioning at pressures up to 3.4 GPa, *Geochem. Geophys. Geosyst.*, *3*(7), 1–23, doi:10.1029/2001GC000148.

Schouten, H., M. A. Tivey, D. J. Fornari, and J. R. Cochran (1999), Central anomaly magnetization high: constraints on the volcanic construction and architecture of seismic layer 2A at a fast-spreading Mid-Ocean Ridge, the EPR at 9°30'-50'N, *Earth Planet. Sci. Lett.*, *169*, 37–50.

Schouten, H., M. A. Tivey, D. J. Fornari, D. Yoeger, A. Bradley, M. Edwards, P. Johnson, Ship Board Science and Technical Teams (2001), Near-bottom investigations of the central anomaly magnetic high (CAMH) at the East Pacific Rise 9°25'-57'N, Cruise Report R/V Atlantis Voyage 7 Leg 4, 11/05–12/04/2001, AT7-4 Cruise Report. [Available at http://imina.soest.hawaii.edu/HMRG/EPR/index.htm, accessed 12 Apr 2013].

Schouten, H., M. A. Tivey, D. J. Fornari, D. R. Yoerger, A. M. Bradley, P. Johnson, M. H. Edwards, and T. Kurokawa (2002), Lava transport and accumulation processes on EPR 9°27'N to 10°N: interpretations based on recent near-bottom sonar imaging and seafloor observations using ABE, Alvin, and a new digital deep sea camera, *Eos Trans*. AGU, 83, T11C-1262.

Schouten, H., M. Tivey, D.J. Fornari, W. Seyfried, and Ship Board Science and Technical Teams (2004), Central anomaly magnetic high and volcanic processes on fast-spreading mid-ocean ridges, Cruise Report R/V Atlantis Voyage 11 Leg 7, 1/26-2/24/2004.

Sigmarrson, O., M. Condomines, K. Gronvold, and T. Thordarson (1991), Extreme magma homogeneity in the 1783-84 Lakagigar eruption: origin of a large volume of evolved basalt in Iceland, *Geophys. Res. Lett.*, *18*(12), 2229–2232.

Sims, K. W. W., et al. (2002), Chemical and isotopic constraints on the generation and transport of melt beneath the East Pacific Rise, *Geochim. Cosmochim. Acta*, *66*, 3481–3504.

Sims, K. W. W., et al. (2003), Aberrant youth: Chemical and isotopic constraints on the origin of off-axis lavas from the East Pacific Rise, 9°–10°N, *Geochem. Geophys. Geosyst.*, *4*(10), 8621, doi:10.1029/2002GC000443.

Sims, K. W. W., S. R. Hart, M. K. Reagan, J. Blusztajn, H. Staudigel, R. A. Sohn, G. D. Layne, L. A. Ball, and J. Andrews (2008a), 238U-230Th-226Ra-210Pb-210Po, 232Th-226Ra, and 235U-231Pa constraints on the ages and petrogenesis of Vailulu'u and Malumalu Lavas, Samoa, *Geochem. Geophys. Geosyst.*, *9*, Q04003, doi:10.1029/2007GC001651.

Sims, K. W. W., et al. (2008b), An inter-laboratory assessment of the thorium isotopic composition of synthetic and rock reference materials, *Geostand Geoanal. Res.*, *32*, 65–91.

Sinton, J., E. Bergmanis, K. Rubin, R. Batiza, T. K. P. Gregg, K. Gronvold, K. C. Macdonald, and S. M. White (2002), Volcanic eruptions on mid-ocean ridges: New evidence from the superfast spreading East Pacific Rise, 17°–19°S, *J. Geophys. Res.*, *107*(B6), ECV3-1– ECV3–20, doi:10.1029/2000JB000090.

Sohn, R. A. (2005), A general inversion for end-member ratios in binary mixing systems, *Geochem. Geophys. Geosyst.*, *6*, Q11007, doi:10.1029/2005GC000975.

Sohn, R. A., and W. Menke (2002), Application of maximum likelihood and bootstrap methods to nonlinear curve-fit problems in geochemistry, *Geochem. Geophys. Geosyst.*, *3*(7), 1–17, doi:10.1029/2001GC000253.

Sohn, R. A., S. C. Webb, and J. A. Hildebrand (2004), Fine-scale seismic structure of the shallow volcanic crust on the East Pacific Rise at 9°50'N, *J. Geophys. Res.*, *109*, B12104, doi:10.1029/2004JB003152.

Soule, S. A., D. J. Fornari, M. R. Perfit, M. A. Tivey, W. I. Ridley, and H. Schouten (2005), Channelized lava flows at the East Pacific Rise crest 9°–10°N: the importance of off-axis lava transport in developing the architecture of young oceanic crust, *Geochem. Geophys. Geosyst.*, *6*, Q08005, doi:10.1029/2005GC000912.

Soule, S. A., D. J. Fornari, M. R. Perfit, and K. H. Rubin (2007), New insights into mid-ocean ridge volcanic processes from the 2005–2006 eruption of the East Pacific Rise, 9°46'N-9°56'N, *Geology*, *35*(12), 1079–1082, doi:10.1130/G23924A.1.

Soule, S. A., J. Escartín, and D. J. Fornari (2009), A record of eruption and intrusion at a fast spreading ridge axis: Axial summit trough of the East Pacific Rise at 9–10°N, *Geochem. Geophys. Geosyst.*, *10*, Q10T07, doi:10.1029/2008GC002354.

Spiegelman, M., and T. Elliot (1993), Consequences of melt transport for uranium series disequilibrium in young lavas, *Earth Planet. Sci. Lett. 118*, 1–20.

Standish, J. J., and K. W. W. Sims (2010), Young off-axis volcanism along the ultraslow-spreading Southwest Indian Ridge, *Nature Geosci.*, *3*, 286–292.

Stracke, A., and B. Bourdon (2009), The importance of melt extraction for tracing mantle heterogeneity, *Geochim. Cosmochim. Acta*, *73*, 218–238.

Sturm, M. E., S. J. Goldstein, E. M. Klein, J. A. Karson, and M. T. Murrell (2000), Uranium-series age constraints on lavas from the axial valley of the Mid-Atlantic Ridge, MARK area, *Earth Planet. Sci. Lett.*, *181*, 61–70.

Thordarson, T., and S. Self (1993), The Laki (Skaftar Fires) and Grimsvotn eruptions, *Bull. Volcanol.*, *55*, 233–263.

Thurber, D. (1962), Anomalous 234U/238U in nature, *J. Geophys. Res.*, *67*, 4518.

Turner, S., C. Beier, Y. Niu, and C. Cook (2011), U-Th-Ra disequilibria and the extent of off-axis volcanism across the East Pacific Rise at 9°30'N, 10°30'N, and 11°20'N, *Geochem. Geophys. Geosyst.*, *12*, Q0AC12, doi:10.1029/2010GC003403.

Vera, E. E., and J. B. Diebold (1994), Seismic imaging of oceanic layer 2A between 9°30 and 10°N on the East Pacific Rise from two ship wide-aperture profiles, *J. Geophys. Res.*, *99*, 3031–3041.

Volpe, A. M., and S. J. Goldstein (1993), 226Ra-230Th disequilibrium in axial and off-axis mid-ocean ridge basalts, *Geochim. Cosmochim. Acta*, *57*, 1233–1242.

Waters, C. L., K. W. W. Sims, M. R. Perfit, J. Blichert-Toft, and J. Blusztajn (2011), Perspective on the genesis of E-MORB from chemical and isotopic heterogeneity at 9–10°N East Pacific Rise, *J. Petrol.*, *52*(3), 565–602, doi:10.1093/petrology/egq091.

White, S. M., R. M Haymon, D. J. Fornari, M. R. Perfit, and K. C. Macdonald (2002), Correlation between volcanic and

tectonic segmentation of fast-spreading ridges: evidence from volcanic structures and lava morphology on the East Pacific Rise, 9°–10°N, *J. Geophys. Res.*, *107*(B8), 2173, doi:10.1029/2001JB000571.

White, S. M., R. M. Haymon, and S. Carbotte (2006), A new view of ridge segmentation and near-axis volcanism at the East Pacific Rise, 8°–12°N, from EM300 multibeam bathymetry, *Geochem. Geophys. Geosyst.*, *7*, Q12O05, doi:10.1029/2006GC001407.

Williams, C. M., M. A. Tivey, H. Schouten, and D. J. Fornari (2008), Central Anomaly Magnetization High documentation of crustal accretion along the East Pacific Rise (9°55′N–9°25′N), *Geochem. Geophys. Geosyst.*, *9*, Q04015, doi:10.1029/2007GC001611.

Zindler, A., H. Staudigel, and R. Batiza (1984), Isotope and trace element geochemistry of young Pacific seamounts: implications for the scale of upper mantle heterogeneity, *Earth Planet. Sci. Lett.*, *70*, 175–195.